S1 Full model domain

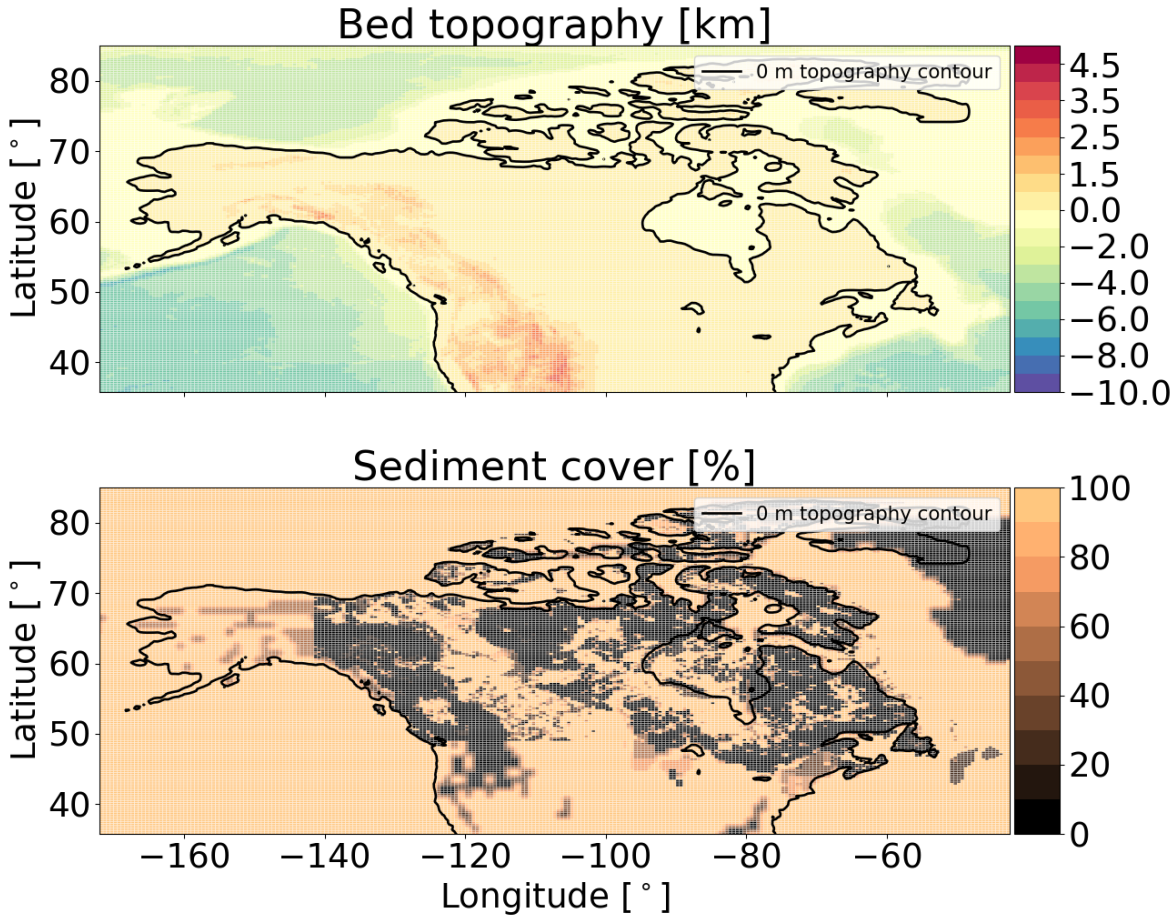

Figure S1. GSM input present-day bed topography and sediment cover for the full model domain. The black contour line shows the present-day sea level (coastline) used in the GSM. Note the change in the color bar step at 0 km.

S2 Ensemble parameter ranges

Number - Definition	Parameter	initial range	range of sieved ensemble	scaling and unit
01 - Weertman soft-bed sliding coefficient	C_{rmu} (Eq. 2)	$0.10 \rightarrow 2.00$	$0.25 \rightarrow 1.90$	$R \cdot \frac{3\ \mathrm{m\,yr^{-1}}}{(30\ \mathrm{kPa})^{n_{\mathrm{b,soft}}}}$
02 - hard-bed sliding coefficient	C_{fslid} (Eq. 2)	$0.20 \rightarrow 4.99$	$0.24 \rightarrow 4.98$	$R \cdot \frac{3\ \mathrm{m\,yr^{-1}}}{(30\ \mathrm{kPa})^4}$
03 - calving coefficent	fcalvin	$0.10 \rightarrow 0.70$	$0.39 \rightarrow 0.65$	$R \cdot 10\ \mathrm{km\,yr^{-1}}$
04 - hydrofracturing coefficient	pfactdwCrack	$0.51 \rightarrow 4.00$	$0.67 \rightarrow 3.96$	$R \cdot 100$
05 - face melt coefficient	C_{face} (Eq. 9)	$0.50 \rightarrow 4.00$	$0.54 \rightarrow 2.88$	$R \cdot 10\ \mathrm{m\,yr^{-1}}$
06 - sub-shelf melt coefficient	C_{SSM} (Eq. 8)	$0.00 \rightarrow 0.80$	$0.00 \rightarrow 0.71$	$R \cdot 16 + 2$
07 - marine freezing point (effective bias adjustment)	TssmCut	$0.00 \rightarrow 1.00$	$0.12 \rightarrow 0.98$	$-R \cdot 4^{\circ}\mathrm{C}$
08 - global precipitation scale factor for PMIP component	fnpre	$0.80 \rightarrow 1.80$	$0.88 \rightarrow 1.73$	
09 - precipitation orographic forcing regularization	pREG	$0.00 \rightarrow 1.00$	$0.06 \rightarrow 0.99$	$1 \cdot 10^{-3} \cdot 40^{R}$
10 - coefficient for exponential surface temperature dependence of non-PMIP precipitation	fhPRE	$0.03 \rightarrow 0.97$	$0.05 \rightarrow 0.66$	$R \cdot 0.1$
11 - precipitation glacial index phase factor	fnPdexp	$0.51 \rightarrow 1.94$	$0.80 \rightarrow 1.48$	
12 - global LGM temperature scale factor	fnTdfscale	$0.75 \rightarrow 1.25$	$1.03 \rightarrow 1.23$	
13 - temperature glacial index phase factor	fnTdexp	$0.75 \rightarrow 1.25$	$0.75 \rightarrow 1.05$	
14 - desert-elevation exponent	desFac	$0.50 \rightarrow 2.00$	$0.51 \rightarrow 1.91$	
15 - default desert-elevation cutoff	des2	$0.50 \rightarrow 3.00$	$0.52 \rightarrow 2.89$	km
16 - western desert-elevation cutoff	desSW	$0.51 \rightarrow 3.00$	$0.89 \rightarrow 2.80$	km
17 - northwestern desert-elevation cutoff	desNNW	$0.50 \rightarrow 3.00$	$0.84 \rightarrow 2.90$	km
18 - north-central desert-elevation cutoff	desNC	$0.00 \rightarrow 2.50$	$0.01 \rightarrow 2.45$	km
19 - central desert-elevation cutoff	desC	$0.00 \rightarrow 2.50$	$0.08 \rightarrow 2.26$	km
20 - Foxe Basin/Baffin desert-elevation cutoff	desF	$0.00 \rightarrow 2.50$	$0.63 \rightarrow 2.32$	km
21 - Quebec/Labrador desert-elevation cutoff	desQ	$0.50 \rightarrow 3.63$	$0.64 \rightarrow 2.65$	km
22 - south-central desert-elevation cutoff	desSC	$0.00 \rightarrow 2.49$	$0.00 \rightarrow 1.98$	km
23 - south-central precipitation enhancement factor	fmpreSM	$0.00 \rightarrow 1.00$	$0.25 \rightarrow 0.94$	
24 - orographic control parameter	rtdes	$0.00 \rightarrow 1.00$	$0.08 \rightarrow 0.93$	
25 - LGM environmental lapse rate	rlapselgm	$0.00 \rightarrow 1.00$	$0.02 \rightarrow 0.50$	$R \cdot 4^{\circ}\mathrm{C\,km^{-1}} + 4^{\circ}\mathrm{C\,km^{-1}}$
26 - weight of glacially-indexed input GCM precipitation field	fPREweightPMIP	$0.00 \rightarrow 1.00$	$0.02 \rightarrow 0.93$	
27 - principal Empirical Orthogonal Function (pEOF) weight 1	w_{pEOF1}	$0.00 \rightarrow 1.00$	$0.12 \rightarrow 0.98$	$R - 0.5$
28 - pEOF weight 2	w_{pEOF2}	$0.00 \rightarrow 1.00$	$0.16 \rightarrow 0.97$	$R - 0.5$
29 - temporal Empirical Orthogonal Function (tEOF) weight 1	w_{tEOF1}	$0.00 \rightarrow 1.00$	$0.02 \rightarrow 0.57$	$R - 0.5$
30 - tEOF weight 2	w_{tEOF2}	$0.00 \rightarrow 1.00$	$0.35 \rightarrow 0.90$	$R - 0.5$
31 - scaling of EBM temperature field glacial anomaly	fnTEBMscale	$0.90 \rightarrow 1.50$	$0.92 \rightarrow 1.48$	
32 - weight of EBM temperature field	fTweightEBM	$0.00 \rightarrow 1.00$	$0.01 \rightarrow 0.43$	
33 - SW surface melt coefficient	fRadSMB	$0.20 \rightarrow 0.50$	$0.20 \rightarrow 0.48$	$R \cdot 2$
34 - exponent for grid cell fractional sediment cover	fbedpow	$0.00 \rightarrow 1.00$	$0.04 \rightarrow 0.88$	$R \cdot 3.8 + 0.2$
35 - basal drag soft bed subgrid roughness dependency	fSTDtill	$0.00 \rightarrow 1.00$	$0.01 \rightarrow 0.87$	
36 - basal drag hard bed subgrid roughness dependency	fSTDslid	$0.00 \rightarrow 1.00$	$0.03 \rightarrow 0.91$	
37 - soft bed Weertman sliding exponent	$n_{\mathrm{b,soft}}$ (Eq. 1)	$1 \rightarrow 7$	$1 \rightarrow 7$	integer values only
38 - Glen flow law enhancement	fnflow	$2.50 \rightarrow 4.00$	$2.55 \rightarrow 3.69$	
39 - weight of EBM for glacial index setting	rWtEBMindx	$0.00 \rightarrow 1.00$	$0.01 \rightarrow 0.41$	
40 - weight of annual glacial index from ice core records	wtIndxYr	$0.00 \rightarrow 1.00$	$0.06 \rightarrow 0.98$	
41 - ocean temperature glacial index phase factor	rToceanPhase	$0.50 \rightarrow 2.00$	$0.50 \rightarrow 1.97$	
42 - Coulomb-plastic friction coefficient	C_{c} (Eq. 5)	$1.00 \rightarrow 4.60$	$3.12 \rightarrow 4.59$	if $R < 3.1 \rightarrow 0$, else $\rightarrow R - 3$
43 - effective bed roughness scale	$h_{\mathrm{wb,Crit}}$ (Eq. 4)	$0.00 \rightarrow 1.00$	$0.11 \rightarrow 0.98$	$0.01 \cdot 10^{(2R)}\ \mathrm{m}$
44 - constant bed drainage rate	rBedDrainRate	$0.00 \rightarrow 1.00$	$0.01 \rightarrow 0.92$	$10^{R} \cdot 10^{-3}\ \mathrm{m\,yr^{-1}}$
45 - effective-pressure factor	$N_{\mathrm{eff,Fact}}$ (Eq. 3)	$0.00 \rightarrow 1.00$	$0.24 \rightarrow 0.97$	$10^{R} \cdot 2 \cdot 10^{4}\ \mathrm{Pa}$
46 - margin forcing ablation threshold	margbab	$0.00 \rightarrow 0.90$	$0.00 \rightarrow 0.90$	
47 - margin forcing accumulation threshold	margbac	$0.00 \rightarrow 1.00$	$0.00 \rightarrow 0.90$	
48 - margin forcing calving reduction factor	margcalv	$0.02 \rightarrow 1.00$	$0.02 \rightarrow 1.00$	
49 - margin forcing initiation time	fmgpin	$0.90 \rightarrow 0.90$	$0.90 \rightarrow 0.90$	$25\ \mathrm{kyr\ BP} + R \cdot 100\ \mathrm{kyr\ BP}$
50 - thickness of the Lithosphere	d_{L}	$46.0 \rightarrow 146.$	$46.0 \rightarrow 146.$	km
51 - viscosity of the upper mantle	η_{um}	$0.20 \rightarrow 2.00$	$0.20 \rightarrow 2.00$	$10^{21}\ \mathrm{Pa\,s}$
52 - viscosity of the lower mantle	η_{lm}	$1.00 \rightarrow 50.0$	$2.00 \rightarrow 50.0$	$10^{21}\ \mathrm{Pa\,s}$

Table S1. GSM parameter ranges of the initial North American history-matching ensemble (Tarasov et al., in preparation, Tarasov and Goldstein, 2021) and the final sieved ensemble used within this study (20 parameter vectors). The individual parameters are listed following the read-in order of the GSM (matching the input parameter file). R in the last column represents any value within the corresponding parameter range.

S3 Input geothermal heat flux

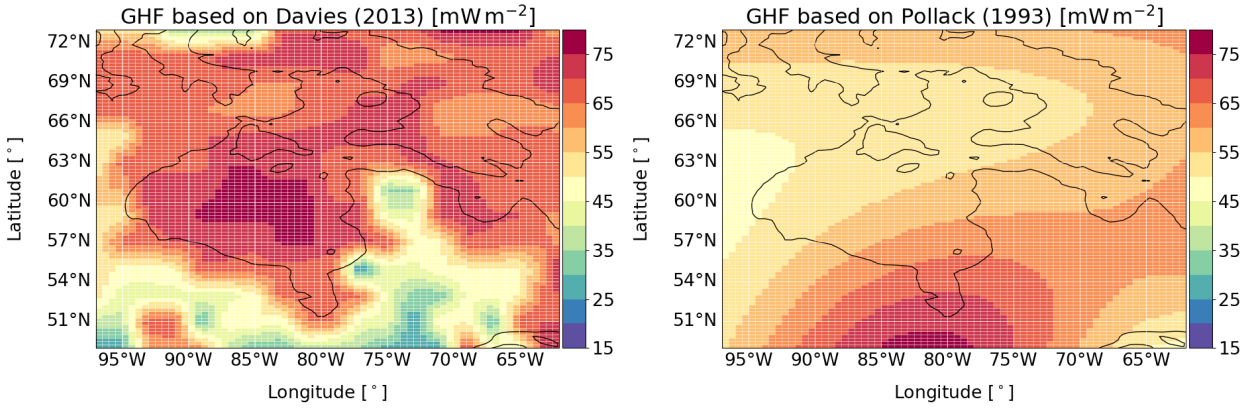

Figure S2. GSM input geothermal heat flux (GHF) applied at 4 km depth. The left panel shows the default input field (Davies, 2013), whereas the right panel shows the GHF based on Pollack et al. (1993). The black contour line shows the present-day sea level used in the GSM.

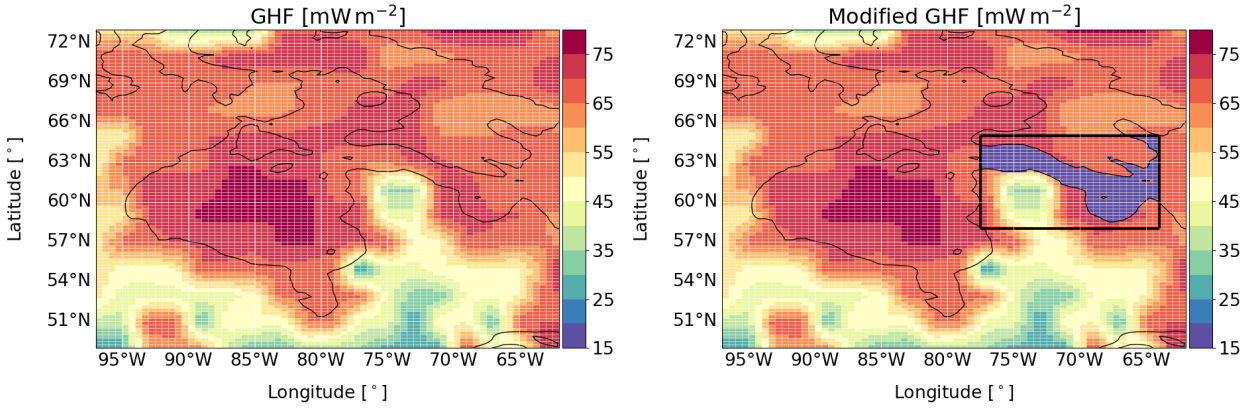

Figure S3. GSM input geothermal heat flux modification for the Hudson Strait area only. Otherwise as Fig. 1.

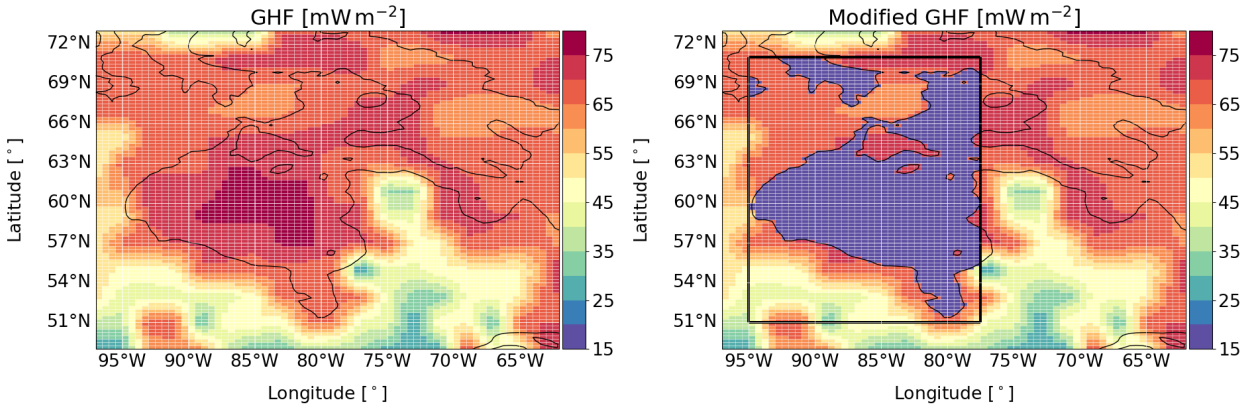

Figure S4. GSM input geothermal heat flux modification for the Hudson Bay area only. Otherwise as Fig. 1.

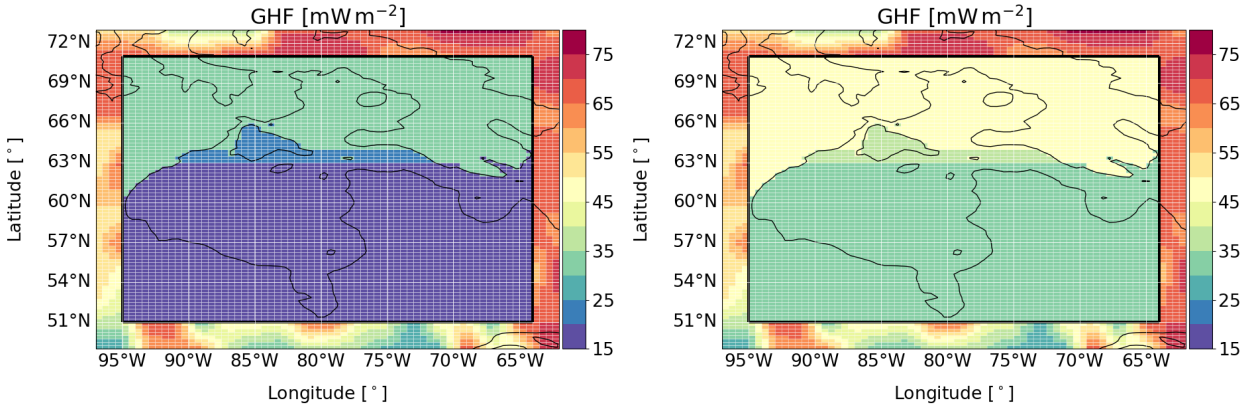

Figure S5. GSM input geothermal heat flux (GHF) applied at 4 km depth. Both panels show GHF maps used to determine the effect of a lower GHF ($\mathrm{GHF_{ave}} \approx 20\,\mathrm{mW\,m^{-2}}$ and $\mathrm{GHF_{ave}} \approx 35\,\mathrm{mW\,m^{-2}}$ in the left and right panel, respectively) when applied to a larger regional area. The GHF was modified based on the GHF map of Blackwell and Richards (2004, reduced values in left panel). Otherwise as Fig. 1.

S4 Hudson Strait ice stream surges

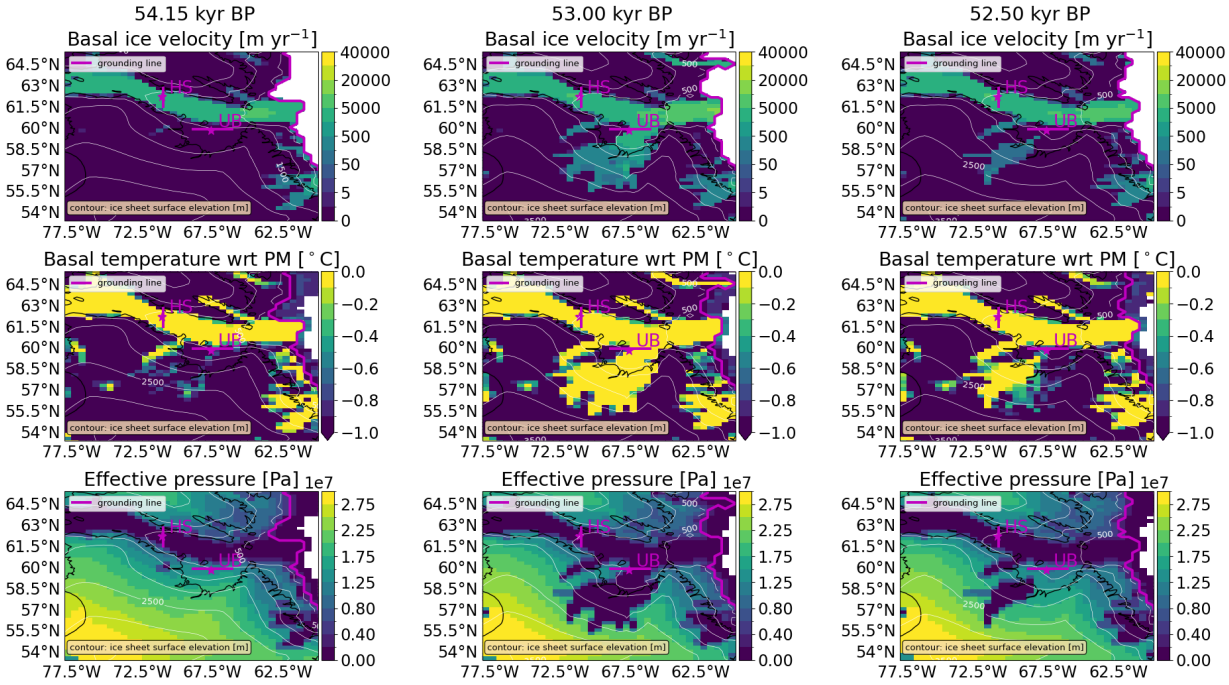

Figure S6. Basal ice velocity, basal temperature with respect to the pressure melting point, and effective pressure for a surge in Ungava Bay. The 3 time slices show the active Hudson Strait ice stream before the Ungava Bay surge (54.15 kyr BP), the Ungava Bay surge (53.00 kyr BP), and the active Hudson Strait ice stream after the Ungava Bay surge (52.50 kyr BP). The black contour is the present-day coastline provided by *cartopy* (Met Office, 2010 - 2015).

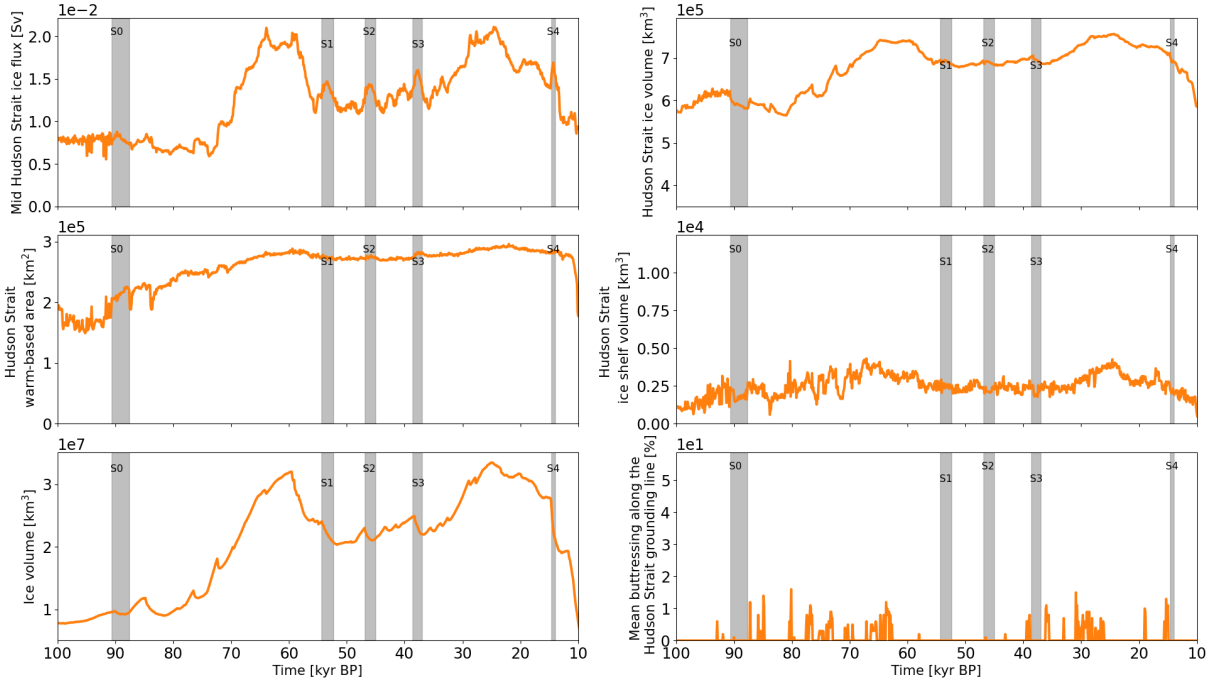

Figure S7. Time series of parameter vector 10. The bottom left panel shows the overall North American ice volume. Otherwise as Fig. 4.

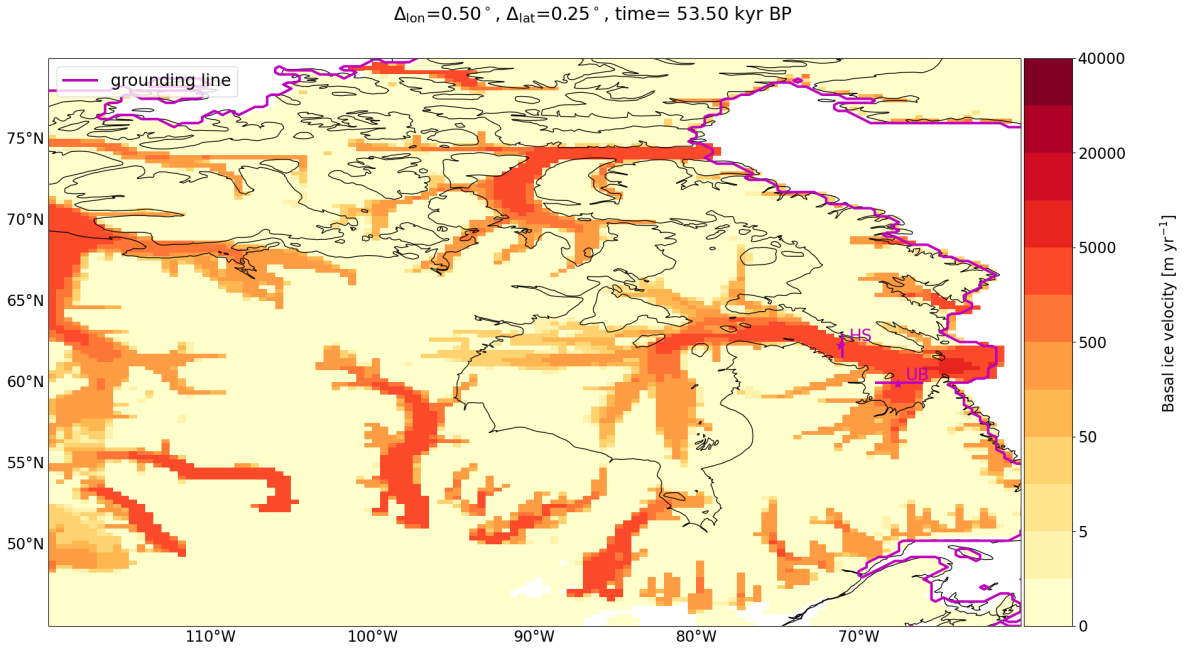

Figure S8. Basal ice velocity during surge S1 for parameter vector 10 in Fig. S7. The black contour is the present-day coastline provided by *cartopy* (Met Office, 2010 - 2015).

S4.1 Timing of Hudson Strait surges

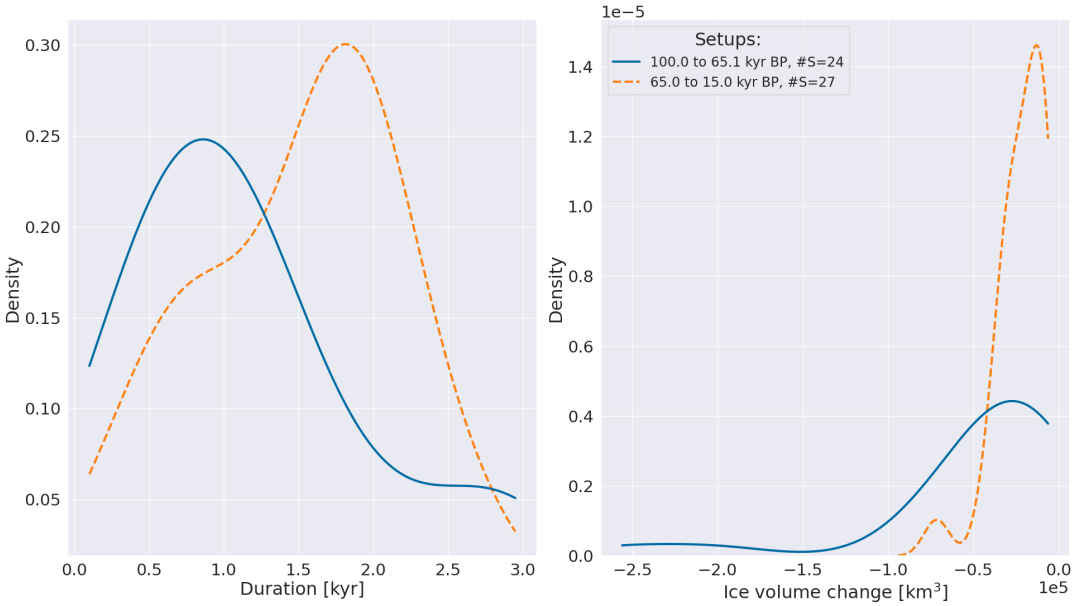

Figure S9. Kernel density plot for the full ensemble (reference setup) and 2 different periods. #S indicates the total number of surges across all runs of the ensemble.

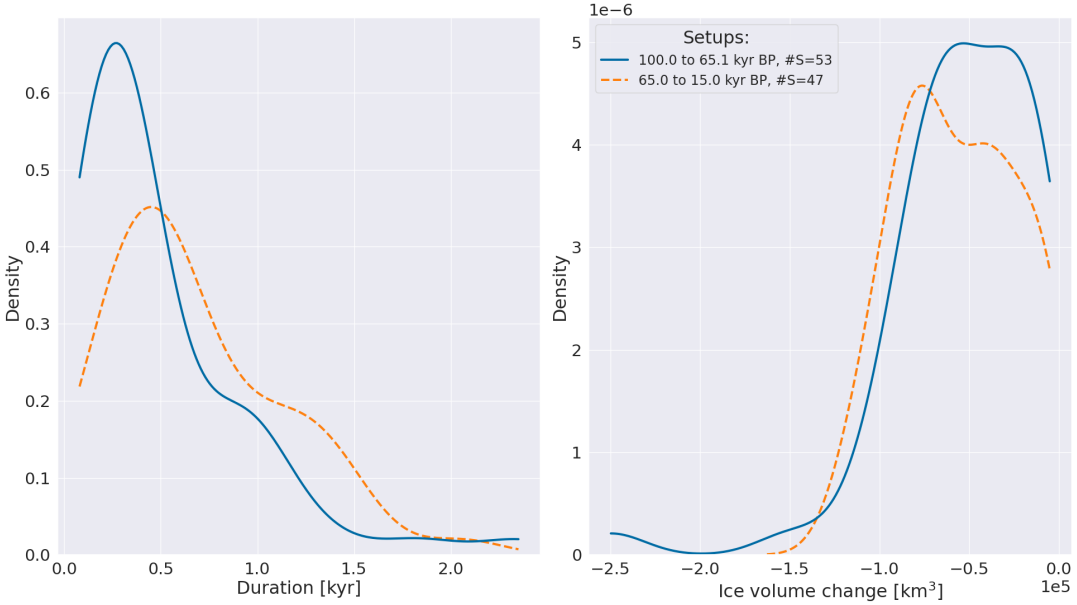

Figure S10. Kernel density plot for the full ensemble of the $\mathrm{GHF_{ave}} = 25\,\mathrm{mW\,m^{-2}}$ experiments and 2 different periods. #S indicates the total number of surges across all runs of the ensemble.

S4.2 Effects of a lower geothermal heat flux

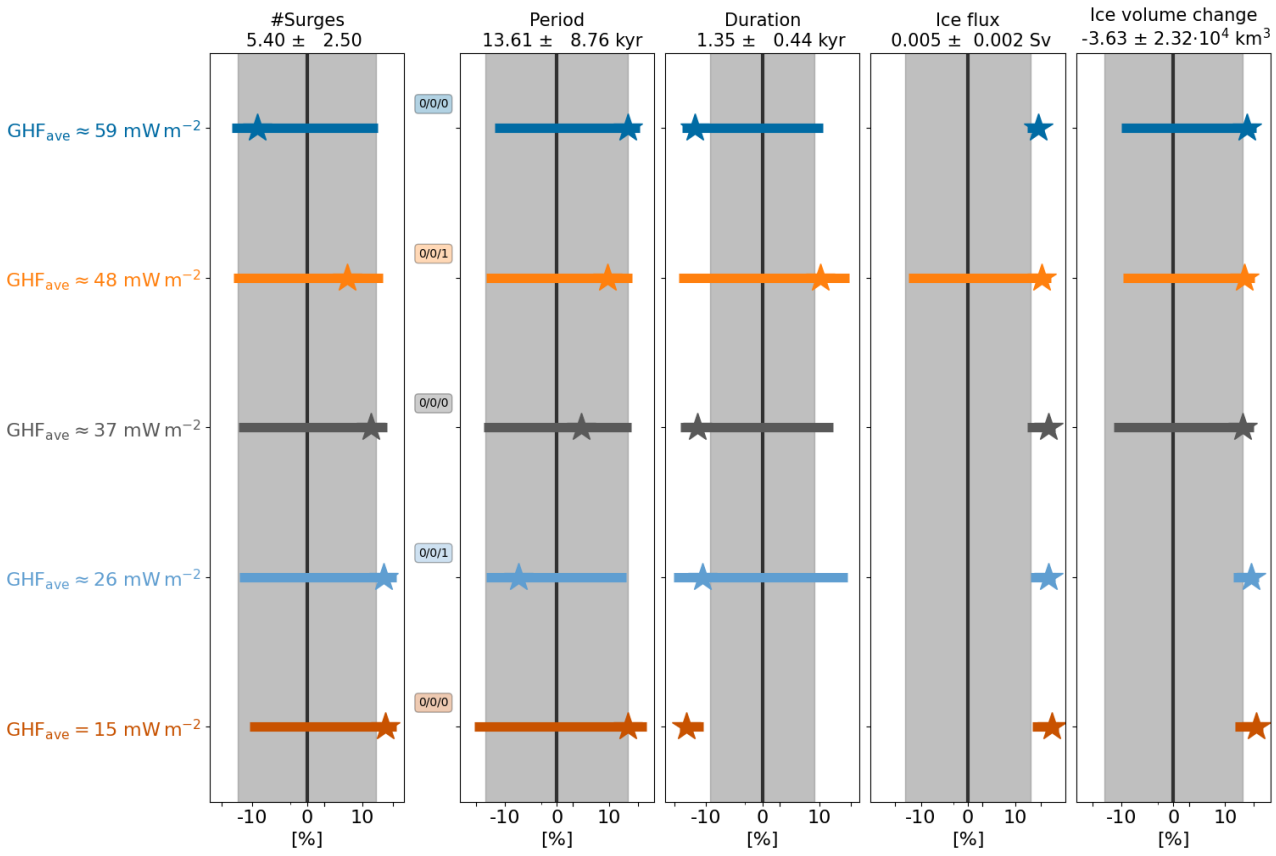

Figure S11. Percentage differences in surge characteristics compared to the reference setup. Only parameter vectors within the > 2 #surges sub-ensemble are considered. The model setups, from top to bottom, are $\mathrm{GHF}_{\mathrm{ave}} \approx [15, 26, 37, 48, 59]\,\mathrm{mW\,m^{-2}}$ (Sec. 2.4). Otherwise as Fig. 6

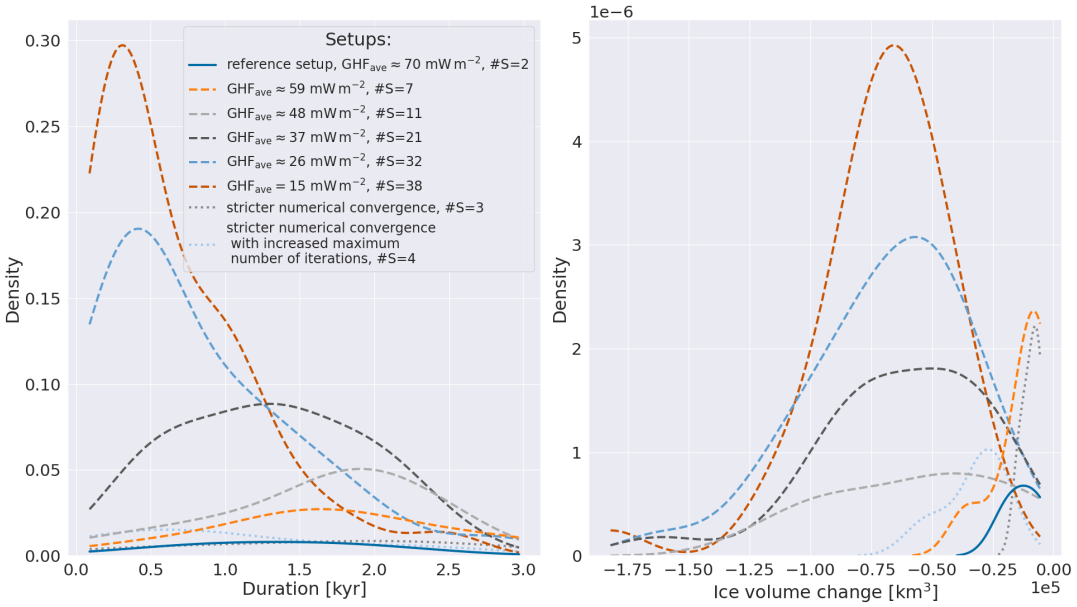

Figure S12. Kernel density plot for the ≤ 2 #surges sub-ensemble. The reference and MNEEs setups use $\mathrm{GHF}_{\mathrm{ave}} \approx 70\,\mathrm{mW\,m^{-2}}$. #S indicates the total number of surges across all runs of the sub-ensemble.

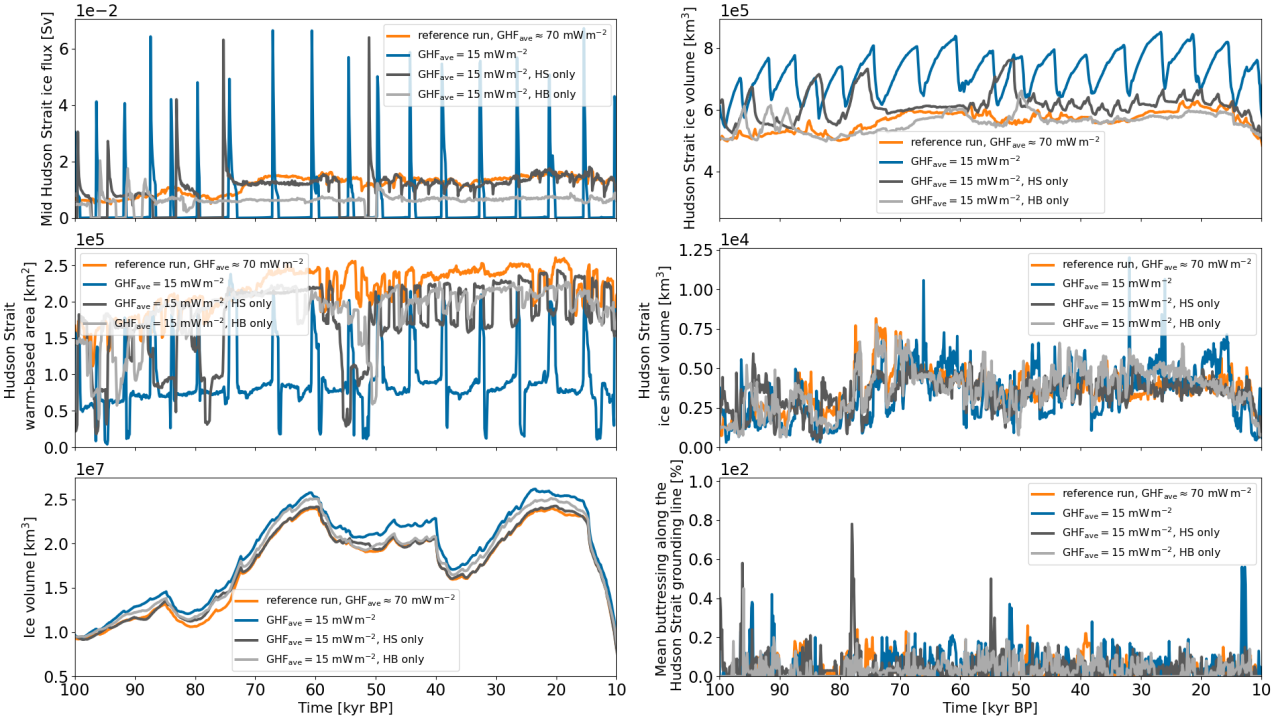

Figure S13. Time series of parameter vector 16 for different GHF modification regions (Sec. 2.4 and Fig. 1, S3, and S4). The Hudson Strait ice stream surges are not highlighted for clarity. The bottom left panel shows the overall North American ice volume. Otherwise as Fig. 4.

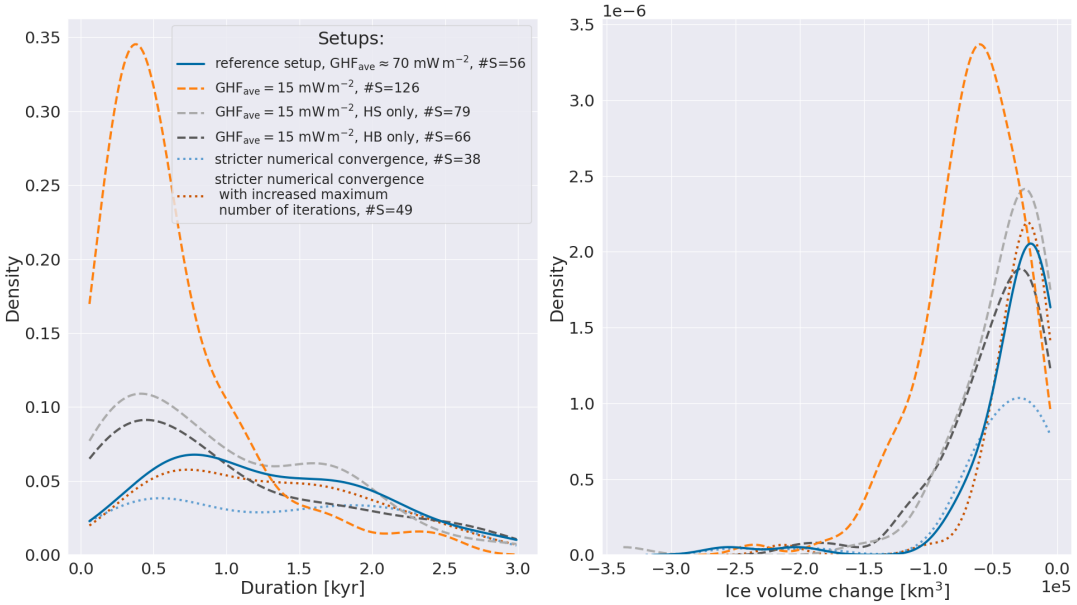

Figure S14. Kernel density plot for the full ensemble. The reference and MNEEs setups use $\mathrm{GHF_{ave}} \approx 70\,\mathrm{mW\,m^{-2}}$. The GHF modification is applied separately to the Hudson Strait (Fig. S3) and Hudson Bay (Fig. S4) for the *HS only* and *HB only* setup, respectively. #S indicates the total number of surges across all runs of the ensemble.

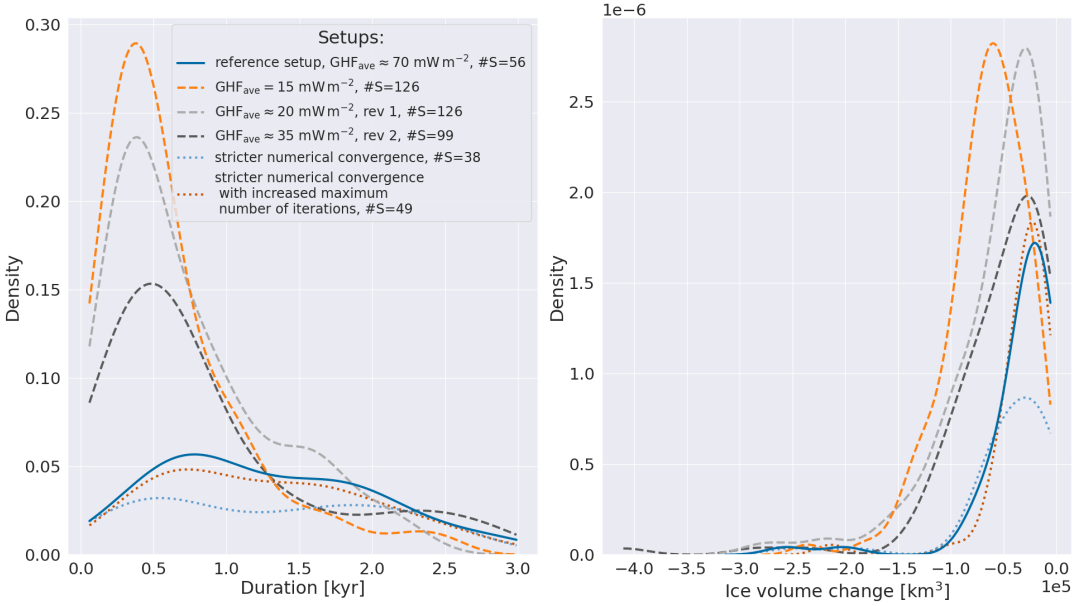

Figure S15. Kernel density plot for the full ensemble. The reference and MNEEs setups use $\mathrm{GHF_{ave}} \approx 70\,\mathrm{mW\,m^{-2}}$. The GHF modification for $\mathrm{GHF_{ave}} = 15\,\mathrm{mW\,m^{-2}}$ is applied to the Hudson Strait and Hudson Bay (Fig. 1). $\mathrm{GHF_{ave}} \approx 20\,\mathrm{mW\,m^{-2}}$, rev 1 and $\mathrm{GHF_{ave}} \approx 35\,\mathrm{mW\,m^{-2}}$, rev 2 use the GHF maps shown in the left and right panels of Fig. S5, respectively. #S indicates the total number of surges across all runs of the ensemble.

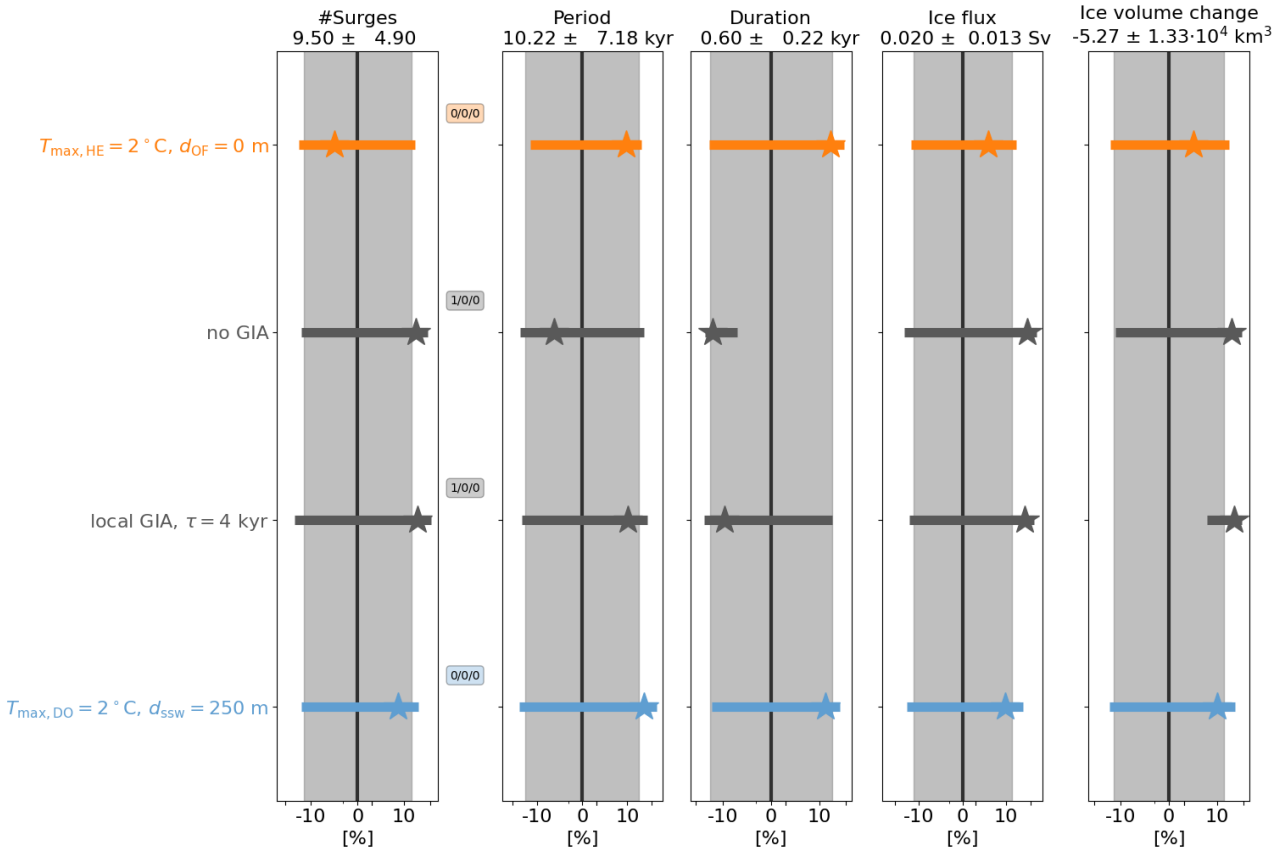

Figure S16. Percentage differences in surge characteristics compared to the $\mathrm{GHF}_{\mathrm{ave}} = 25\,\mathrm{mW\,m^{-2}}$ setup for the > 2 #surges sub-ensemble (11 parameter vectors). All comparison setups also use $\mathrm{GHF}_{\mathrm{ave}} = 25\,\mathrm{mW\,m^{-2}}$. The model setups, from top to bottom, are: Heinrich Event ocean forcing ($T_{\mathrm{max,HE}} = 2°\mathrm{C}$, $d_{\mathrm{OF}} = 250$ m), no GIA model, local GIA model with relaxation time constant $\tau = 4$ kyr, DO event sub-surface ocean forcing with $T_{\mathrm{max,DO}} = 2°\mathrm{C}$. Otherwise as Fig. 6.

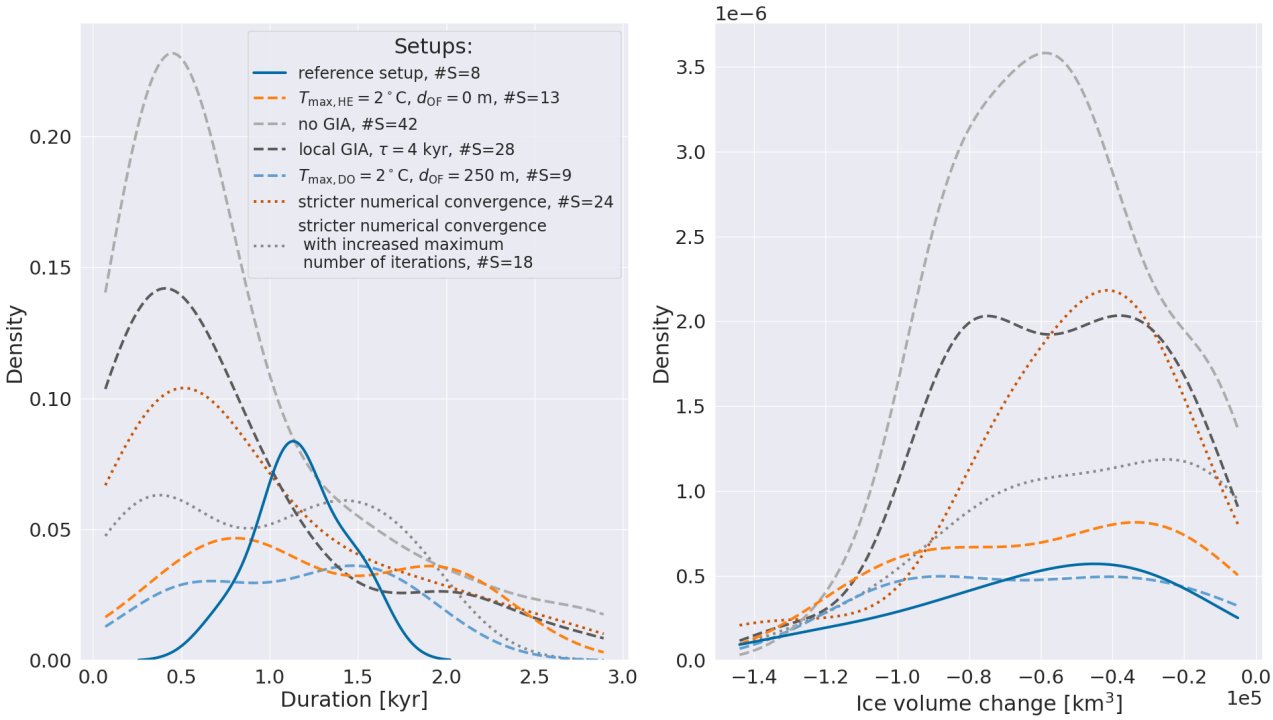

Figure S17. Kernel density plot for the ≤ 2 #surges sub-ensemble (9 parameter vectors) of the $\mathrm{GHF}_{\mathrm{ave}} = 25\,\mathrm{mW\,m^{-2}}$ experiments. #S indicates the total number of surges across all runs of the sub-ensemble.

S4.3 Effects of a different sliding law

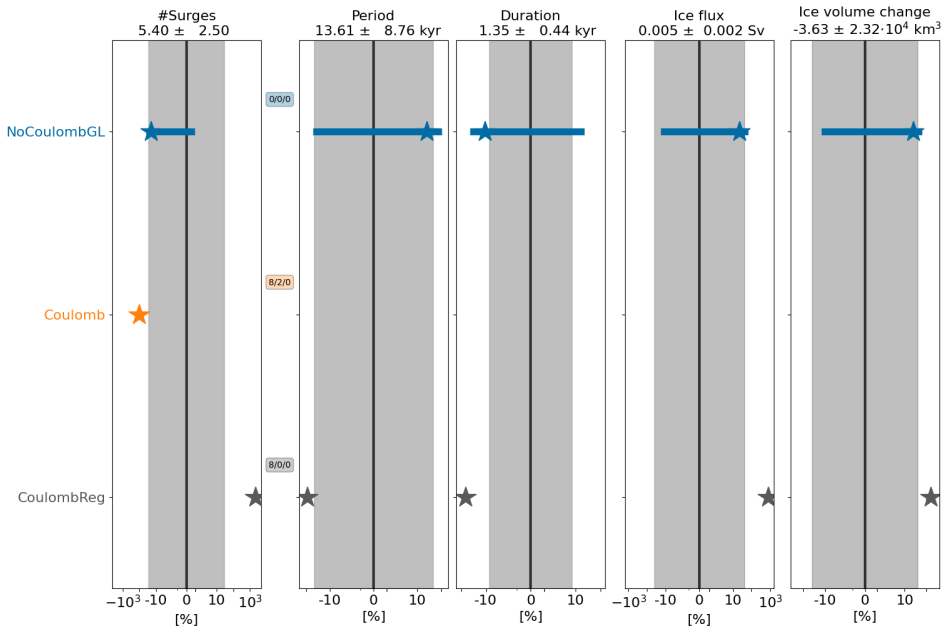

Figure S18. Percentage differences in surge characteristics compared to the reference setup for the > 2 #surges sub-ensemble. The model setups, from top to bottom, are: pure Weertman-type grounding line parameterization ($\tau_{b,GL} = \tau_{b,W}$ instead of Eq. 6), Coulomb friction law (Eq. 5a), and regularized Coulomb friction law (Eq. 5b). Otherwise as Fig. 6.

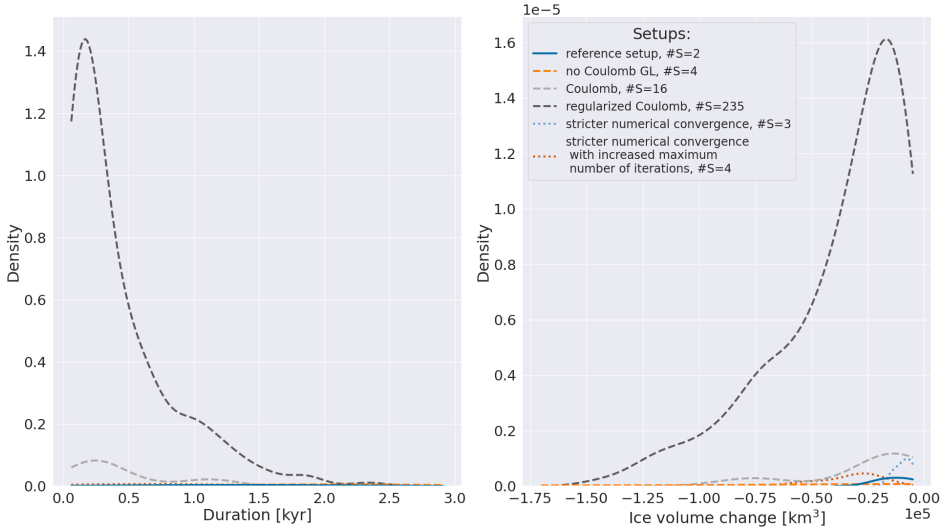

Figure S19. Kernel density plot for the ≤ 2 #surges sub-ensemble. #S indicates the total number of surges across all runs of the sub-ensemble. The model setups, from top to bottom, are: reference setup, pure Weertman-type grounding line parameterization ($\tau_{b,GL} = \tau_{b,W}$ instead of Eq. 6), Coulomb friction law (Eq. 5a), regularized Coulomb friction law (Eq. 5b), and the 2 MNEE experiments.

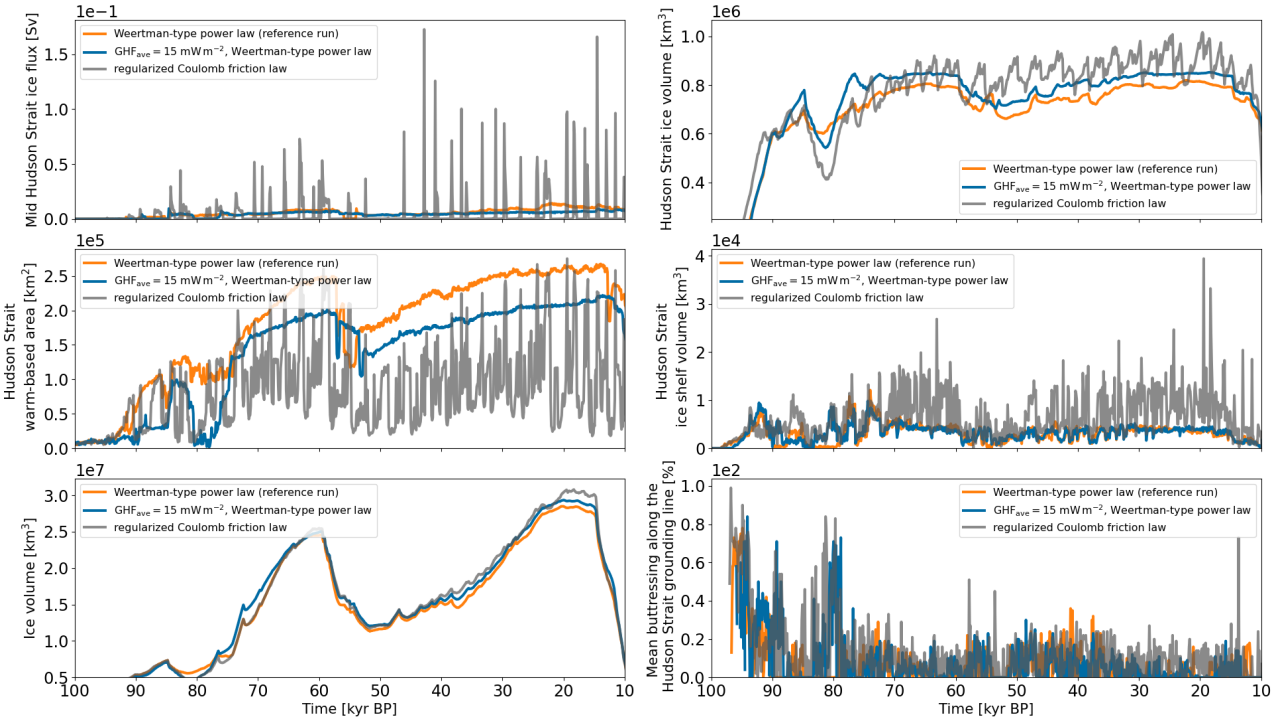

Figure S20. Time series of parameter vector 0 for different sliding laws (Weertman-type power law exponent is 4) and geothermal heat fluxes. The Hudson Strait ice stream surges are not highlighted for clarity. The bottom left panel shows the overall North American ice volume. Otherwise as Fig. 4.

S5 Ocean temperature forcing experiments

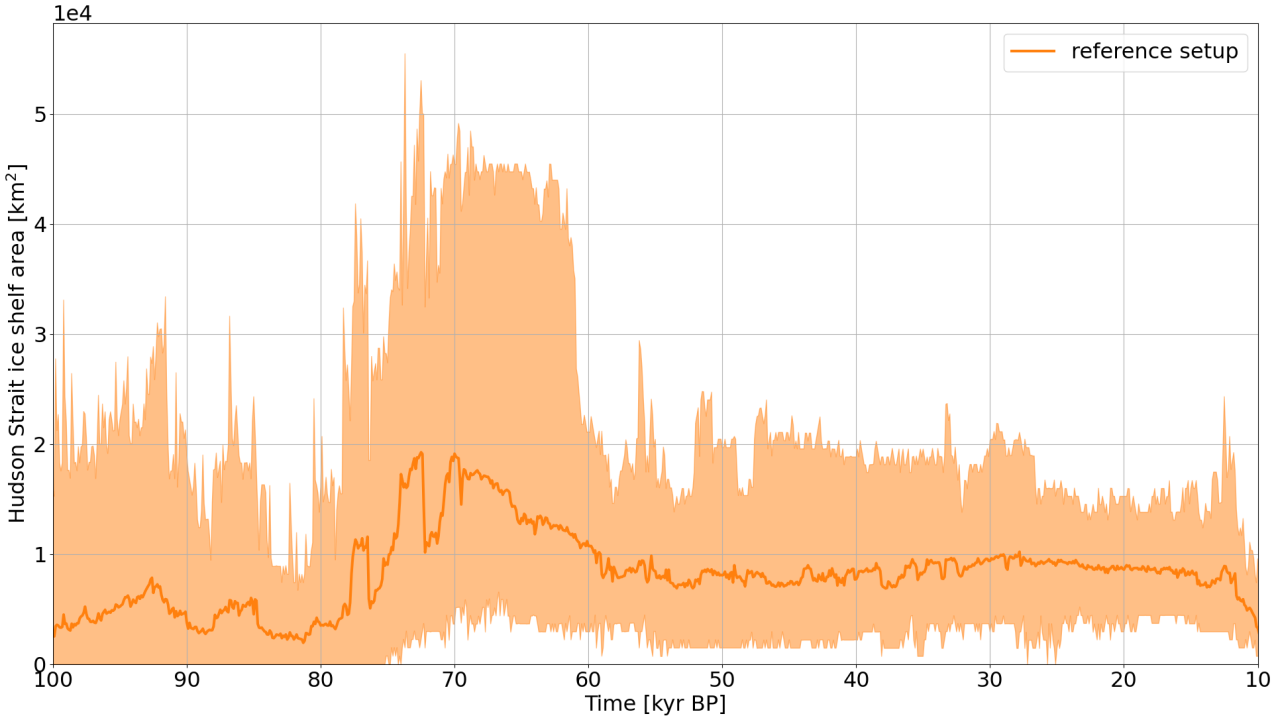

Figure S21. Hudson Strait ice shelf cover in the *Hudson Strait* area outline in Fig. 2 (total area of $\sim 2.6 \cdot 10^5$ km^2). The thick line represents the mean of the 20 run ensemble. The shaded area marks the minimum and maximum of the ensemble.

S5.1 Ice shelf removal

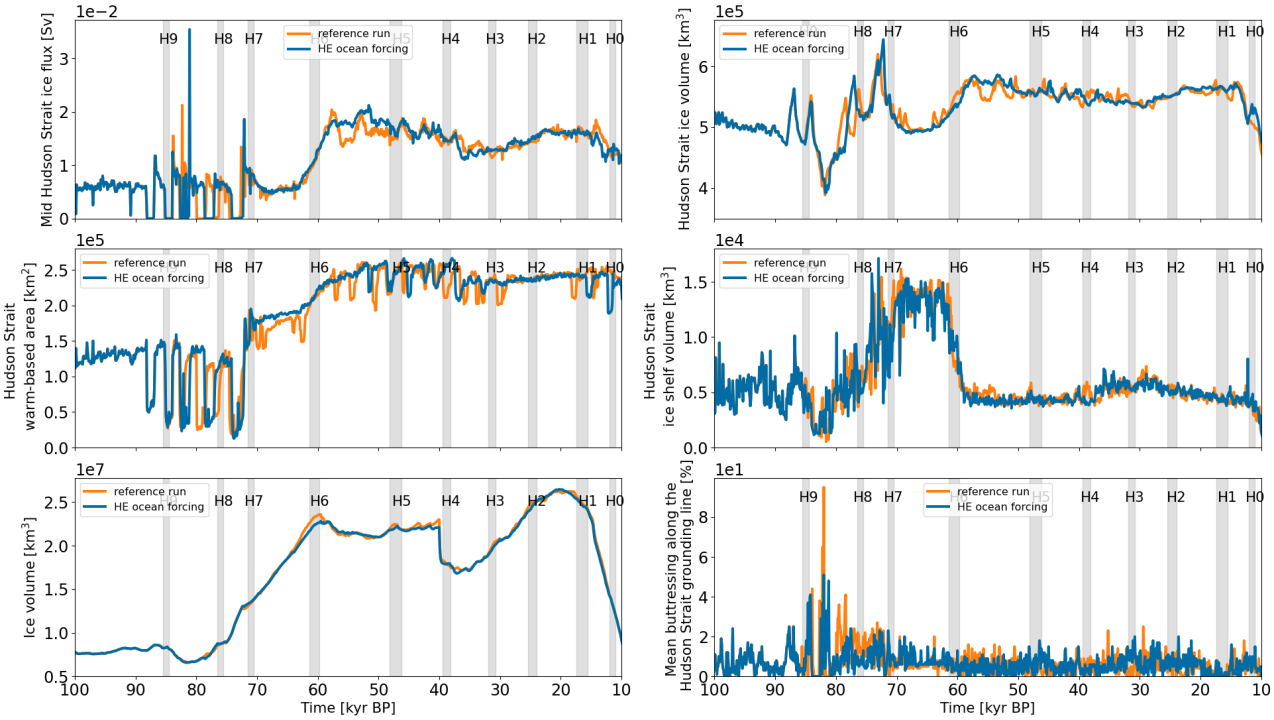

Figure S22. Time series of parameter vector 1 for the reference setup and the ice shelf removal ocean forcing (Sec. 2.5.1). The shaded gray areas mark the HE time estimates based on the average of Table 6.3 in Bradley (2014). The ocean forcing was applied to the whole water column and with a maximum temperature increase of $T_{\max,\mathrm{HE}} = 3°\mathrm{C}$. Otherwise as Fig. 4.

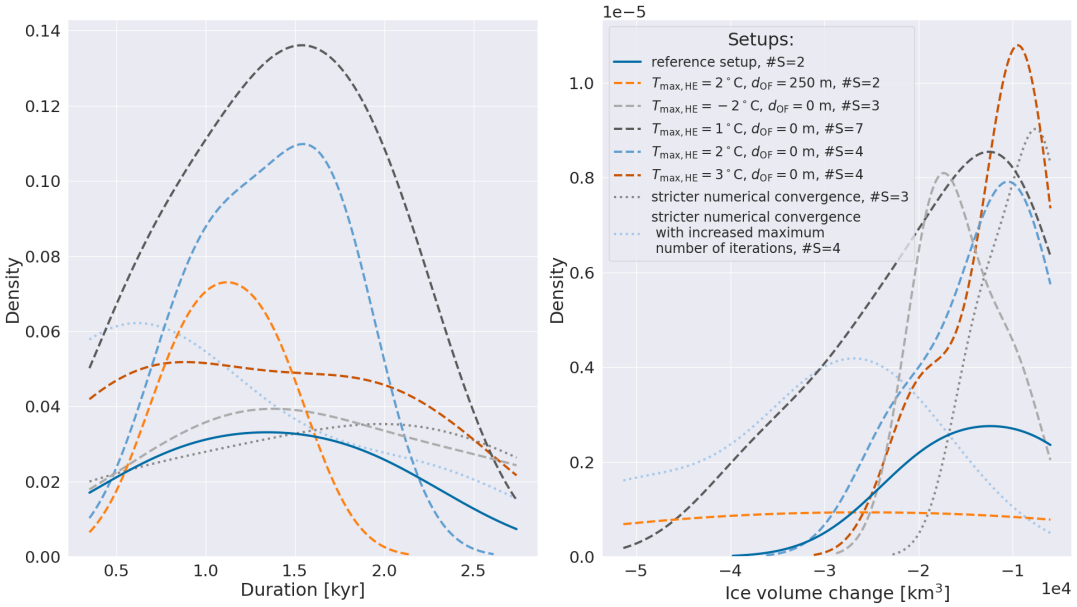

Figure S23. Kernel density plot for the ≤ 2 #surges sub-ensemble. The model setups, from top to bottom, are the reference setup, Heinrich Event ocean forcings (maximum temperature increase $T_{\max,\mathrm{HE}} = 2°\mathrm{C}$, $d_{\mathrm{OF}} = 250$ m), whole water column Heirich Event ocean forcing with $T_{\max,\mathrm{HE}} = [-2, 1, 2, 3]°\mathrm{C}$ (Sec. 2.5.1) and the 2 MNEE experiments. #S indicates the total number of surges across all runs of the sub-ensemble.

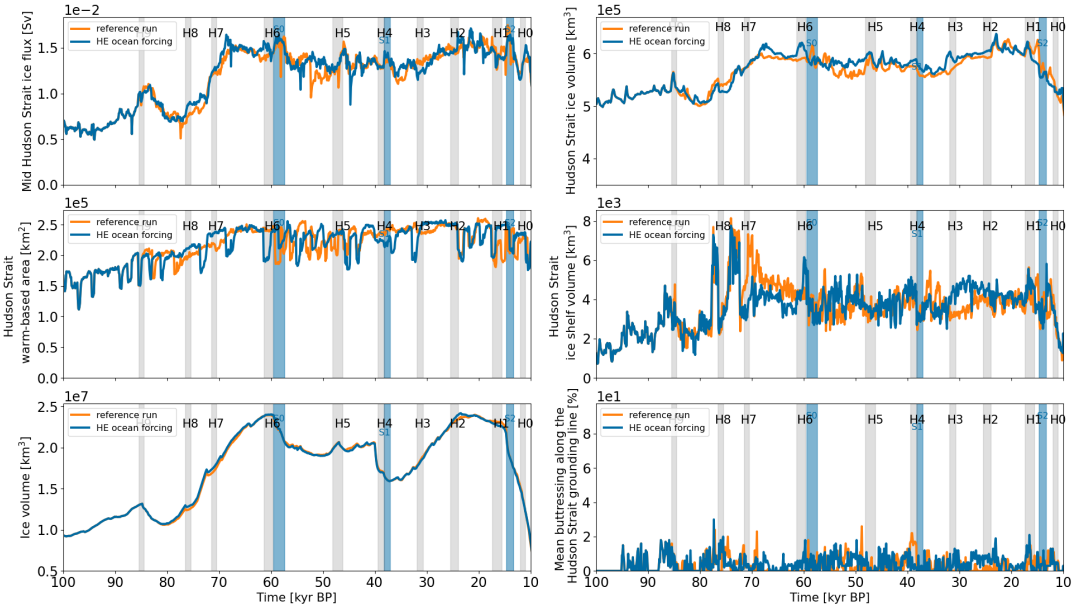

Figure S24. Time series of parameter vector 16 for the reference setup and the ice shelf removal ocean forcing (Sec. 2.5.1). The shaded gray areas mark the HE time estimates based on the average of Table 6.3 in Bradley (2014). The ocean forcing was applied to the whole water column and with a maximum temperature increase of $T_{\max,\mathrm{HE}} = 1°\mathrm{C}$. Otherwise as Fig. 4.

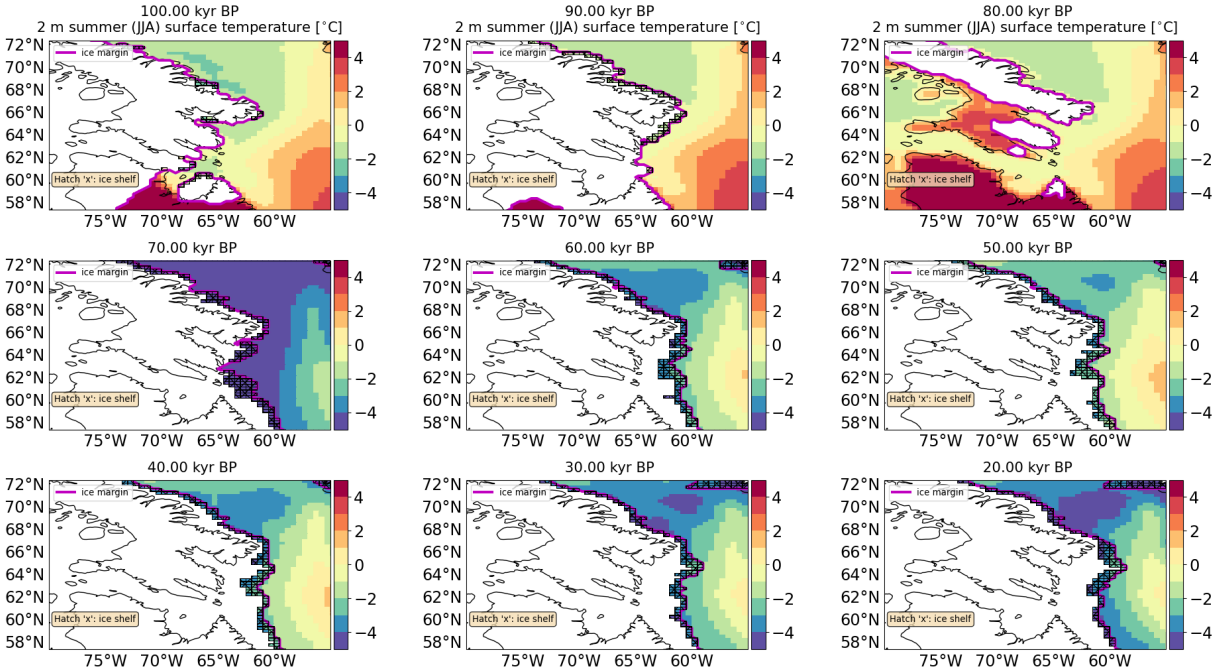

Figure S25. 2 m summer surface temperature for parameter vector 2 (not shown for grid cells with grounded ice). The black contour is the present-day coastline provided by *cartopy* (Met Office, 2010 - 2015).

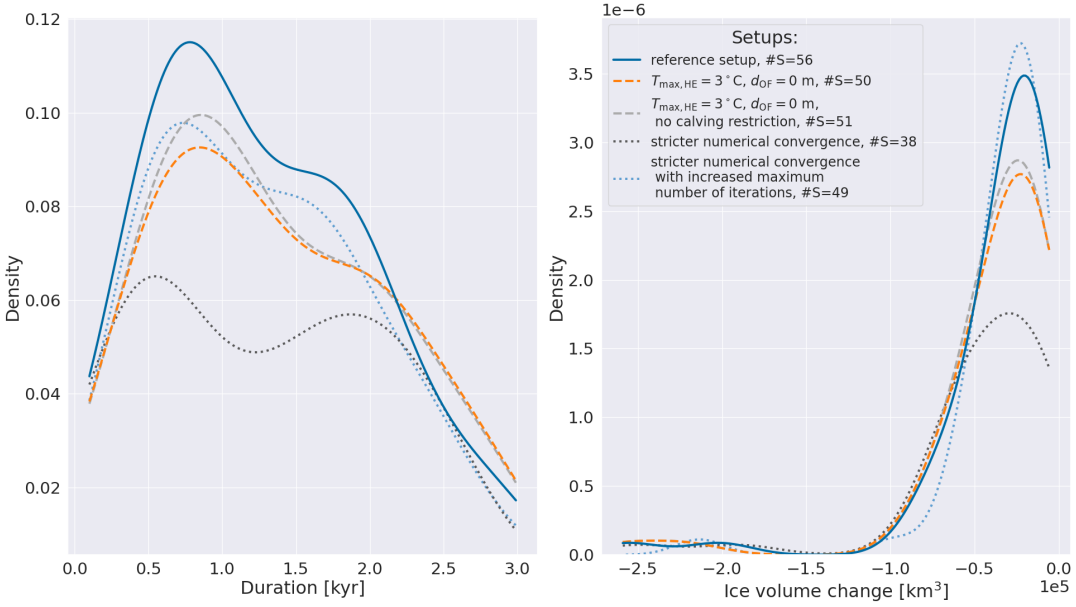

Figure S26. Kernel density plot for the full ensemble. The $T_{\mathrm{max,HE}} = 3°\mathrm{C}$, $d_{\mathrm{OF}} = 0$ m setup inhibits calving when the 2 m summer surface temperature is below $-2.0°\mathrm{C}$ (see Sec. 2.5 for details). #S indicates the total number of surges across all runs of the sub-ensemble.

S5.2 Adding underwater warming pulses

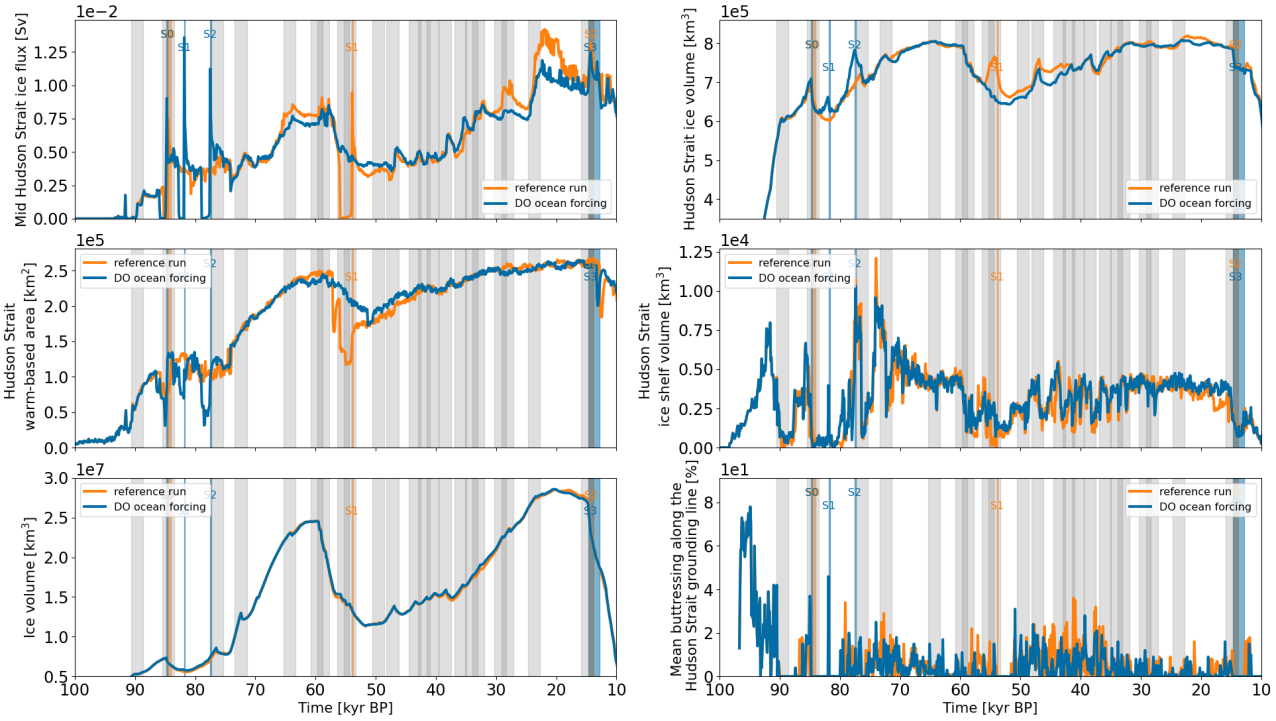

Figure S27. Time series of parameter vector 0 for the reference setup and the sub-surface ocean forcing (Sec. 2.5.2). The shaded gray areas mark the DO event time estimates based on peaks in the NGRIP δ^{18}O time series (Bazin et al., 2013; Veres et al., 2013) with a total duration of $t_{\mathrm{D,tot}} = 2200$ yr (Sec. 2.5.2). The darker gray areas indicate an overlap of sub-surface ocean warmings. The ocean forcing was applied below a water depth $d_{\mathrm{OF}} = 250$ m and with a maximum temperature increase of $T_{\mathrm{max,DO}} = 2°\mathrm{C}$. Otherwise as Fig. 4.

S5.3 Bounding experiments

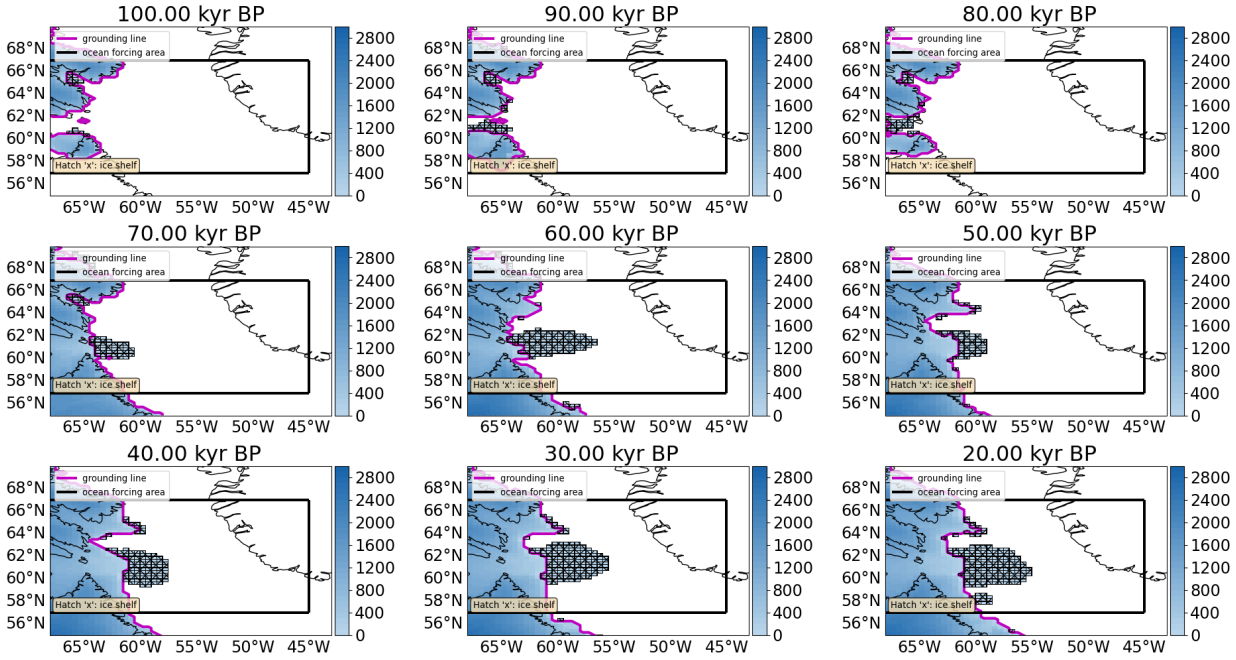

Figure S28. Ice surface elevation in meters for parameter vector 14 and no calving in the *ocean forcing area* (black box, see also Fig. 2). The black contour is the present-day coastline provided by *cartopy* (Met Office, 2010 - 2015).

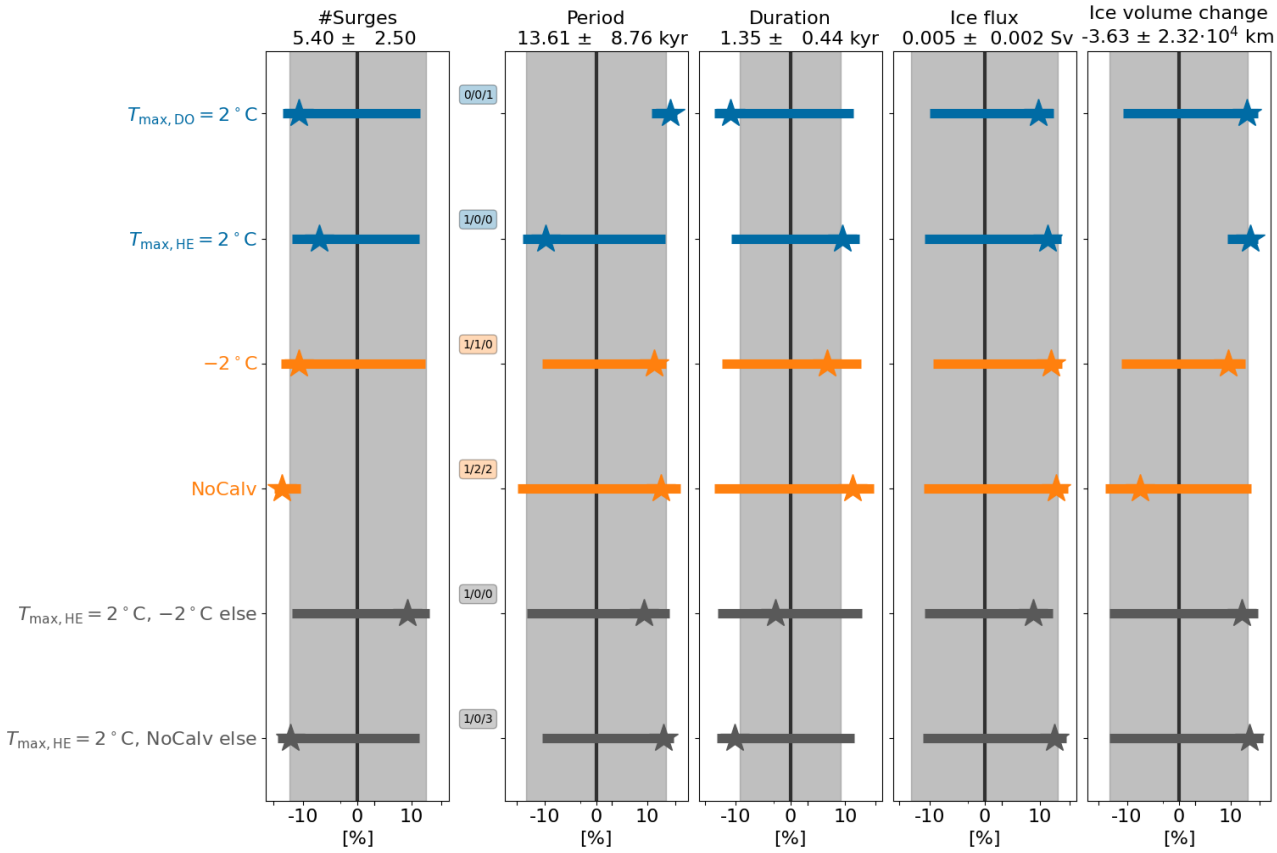

Figure S29. Percentage differences in surge characteristics compared to the reference setup. Only parameter vectors within the > 2 #surges sub-ensemble are considered. The model setups, from top to bottom, are the bounding experiments (Sec. 2.5.3): DO event ocean forcing with maximum temperature increase $T_{\mathrm{max,DO}} = 2°\mathrm{C}$ (BE_1), HE ocean forcing with maximum temperature increase $T_{\mathrm{max,HE}} = 2°\mathrm{C}$ (BE_2), $-2°\mathrm{C}$ ocean temperature decrease applied after 100 kyr BP (BE_3), no calving after 100 kyr BP (BE_4), HE ocean forcing ($T_{\mathrm{max,HE}} = 2°\mathrm{C}$) with $-2°\mathrm{C}$ ocean forcing applied outside of HEs and after 100 kyr BP (BE_5), and HE ocean forcing ($T_{\mathrm{max,HE}} = 2°\mathrm{C}$) with no calving outside of HEs and after 100 kyr BP (BE_6). The ocean forcings are applied for the entire water column and all grid cells within the *ocean forcing area* (not only the ones containing floating ice, Sec. 2.5.3). Otherwise as Fig. 6.

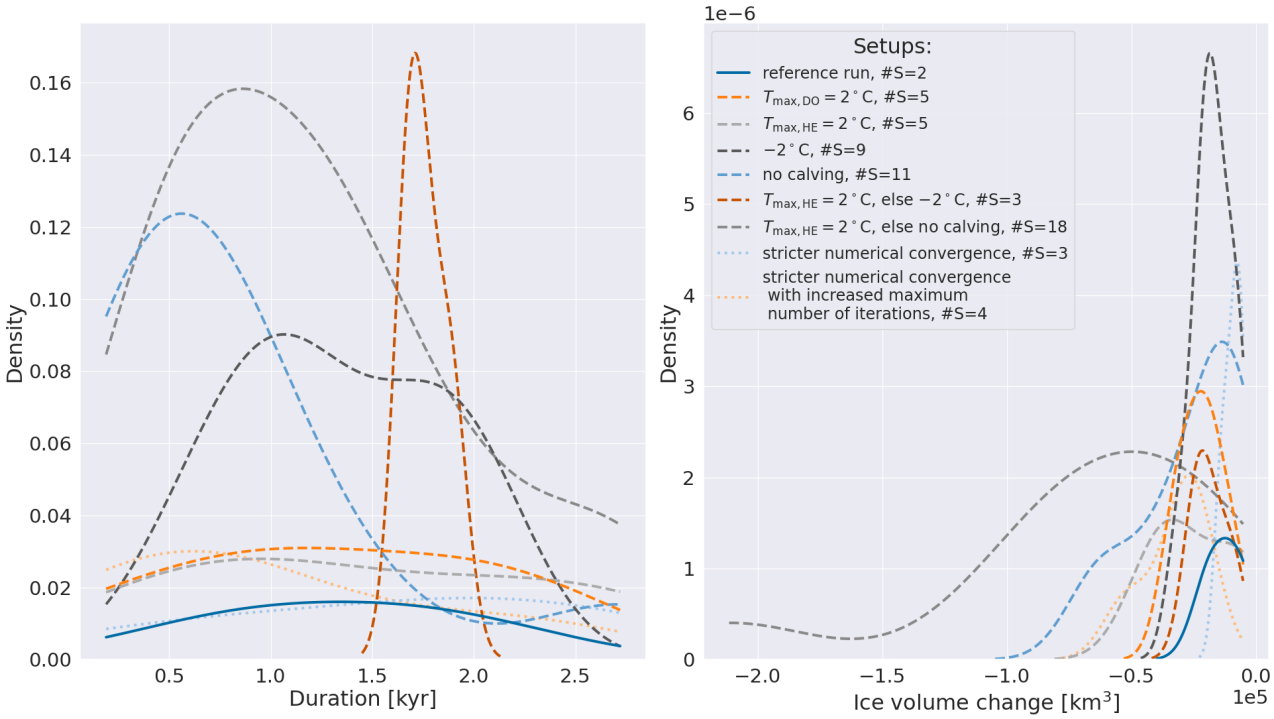

Figure S30. Kernel density plot for the ≤ 2 #surges sub-ensemble. The model setups, from top to bottom, are the reference setup, DO event ocean forcing with maximum temperature increase $T_{\mathrm{max,DO}} = 2^{\circ}\mathrm{C}$ (BE_1), HE ocean forcing with maximum temperature increase $T_{\mathrm{max,HE}} = 2^{\circ}\mathrm{C}$ (BE_2), $-2^{\circ}\mathrm{C}$ ocean temperature decrease applied after 100 kyr BP (BE_3), no calving after 100 kyr BP (BE_4), HE ocean forcing ($T_{\mathrm{max,HE}} = 2^{\circ}\mathrm{C}$) with $-2^{\circ}\mathrm{C}$ ocean forcing applied outside of HEs and after 100 kyr BP (BE_5), HE ocean forcing ($T_{\mathrm{max,HE}} = 2^{\circ}\mathrm{C}$) with no calving outside of HEs and after 100 kyr BP (BE_6), and the 2 MNEE experiments. The ocean forcings are applied for the entire water column and all grid cells within the *ocean forcing area* (not only the ones containing floating ice, Sec. 2.5.3). #S indicates the total number of surges across all runs of the sub-ensemble.

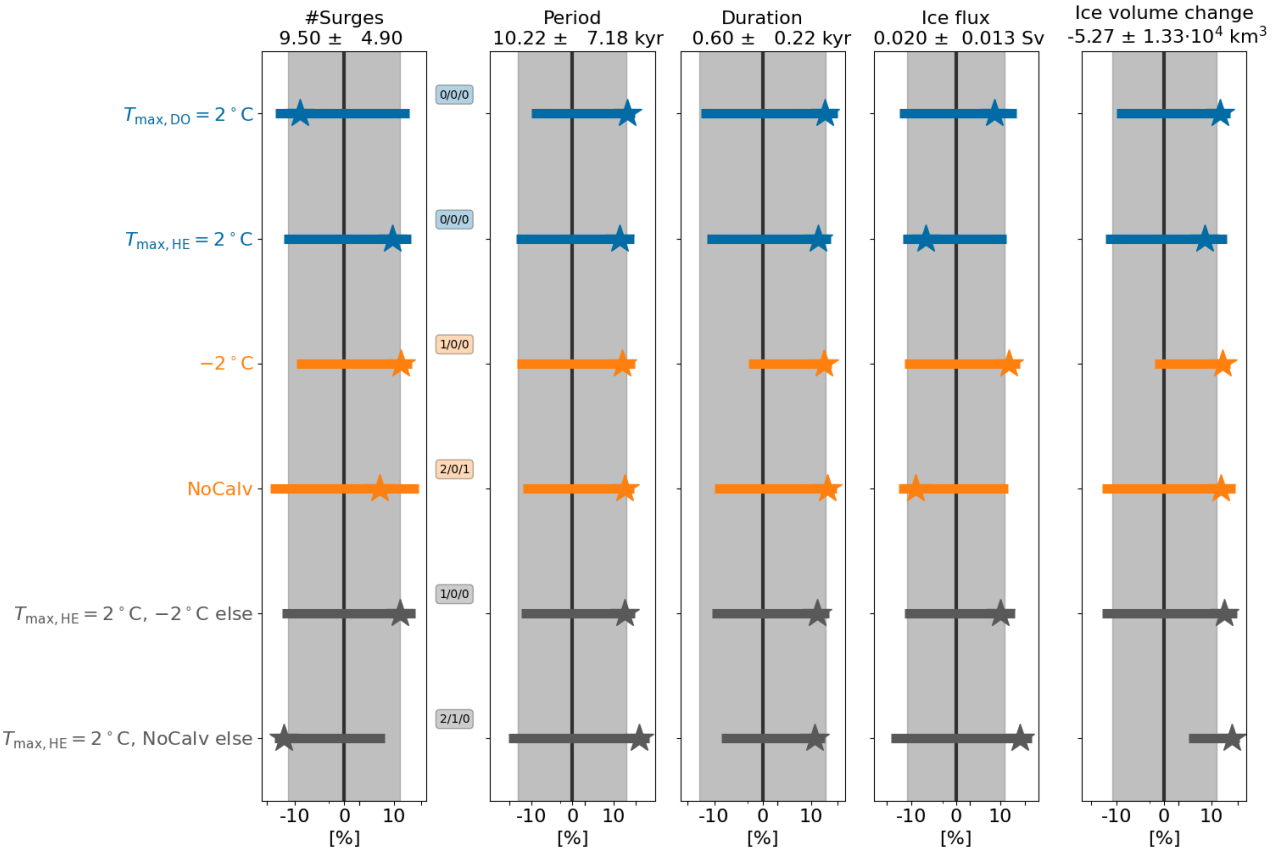

Figure S31. Percentage differences in surge characteristics compared to the $\mathrm{GHF_{ave}} = 25\,\mathrm{mW\,m^{-2}}$ setup for the > 2 #surges sub-ensemble (11 parameter vectors). All comparison setups also use $\mathrm{GHF_{ave}} = 25\,\mathrm{mW\,m^{-2}}$. The model setups, from top to bottom, are the bounding experiments (Sec. 2.5.3): DO event ocean forcing with maximum temperature increase $T_{\mathrm{max,DO}} = 2°\mathrm{C}$ ($\mathrm{BE_1}$), HE ocean forcing with maximum temperature increase $T_{\mathrm{max,HE}} = 2°\mathrm{C}$ ($\mathrm{BE_2}$), $-2°\mathrm{C}$ ocean temperature decrease applied after 100 kyr BP ($\mathrm{BE_3}$), no calving after 100 kyr BP ($\mathrm{BE_4}$), HE ocean forcing ($T_{\mathrm{max,HE}} = 2°\mathrm{C}$) with $-2°\mathrm{C}$ ocean forcing applied outside of HEs and after 100 kyr BP ($\mathrm{BE_5}$), and HE ocean forcing ($T_{\mathrm{max,HE}} = 2°\mathrm{C}$) with no calving outside of HEs and after 100 kyr BP ($\mathrm{BE_6}$). The ocean forcings are applied for the entire water column and all grid cells within the *ocean forcing area* (not only the ones containing floating ice, Sec. 2.5.3). Otherwise as Fig. 6.

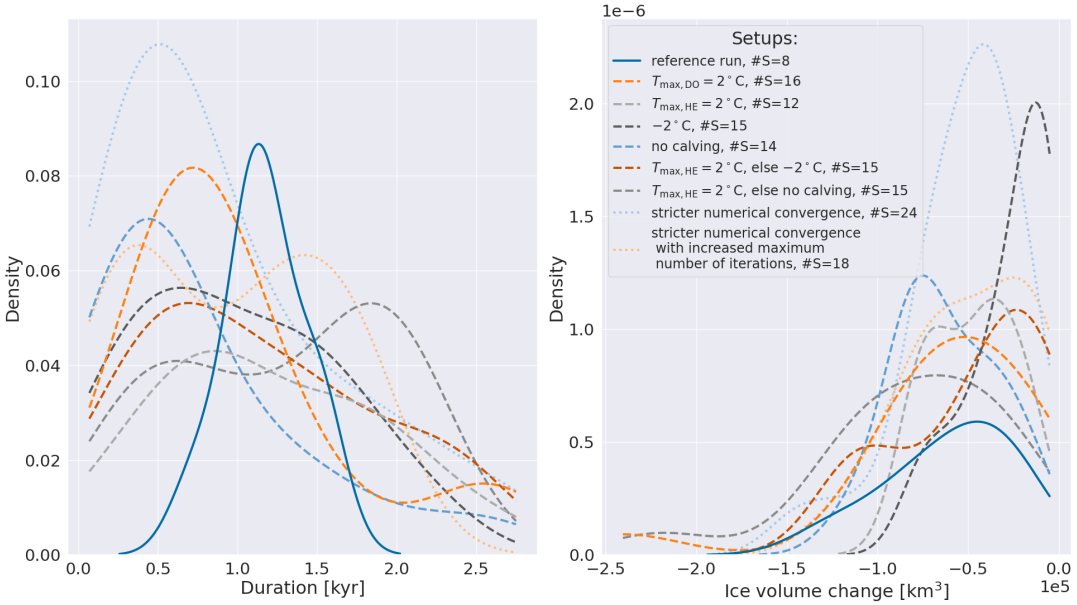

Figure S32. Kernel density plot for the ≤ 2 #surges sub-ensemble with $\mathrm{GHF_{ave}} = 25\,\mathrm{mW\,m^{-2}}$ (9 parameter vectors). The model setups, from top to bottom, are the reference setup, DO event ocean forcing with maximum temperature increase $T_{\mathrm{max,DO}} = 2^{\circ}\mathrm{C}$ (BE_1), HE ocean forcing with maximum temperature increase $T_{\mathrm{max,HE}} = 2^{\circ}\mathrm{C}$ (BE_2), $-2^{\circ}\mathrm{C}$ ocean temperature decrease applied after 100 kyr BP (BE_3), no calving after 100 kyr BP (BE_4), HE ocean forcing ($T_{\mathrm{max,HE}} = 2^{\circ}\mathrm{C}$) with $-2^{\circ}\mathrm{C}$ ocean forcing applied outside of HEs and after 100 kyr BP (BE_5), HE ocean forcing ($T_{\mathrm{max,HE}} = 2^{\circ}\mathrm{C}$) with no calving outside of HEs and after 100 kyr BP (BE_6), and the 2 MNEE experiments. The ocean forcings are applied for the entire water column and all grid cells within the *ocean forcing area* (not only the ones containing floating ice, Sec. 2.5.3). #S indicates the total number of surges across all runs of the sub-ensemble.

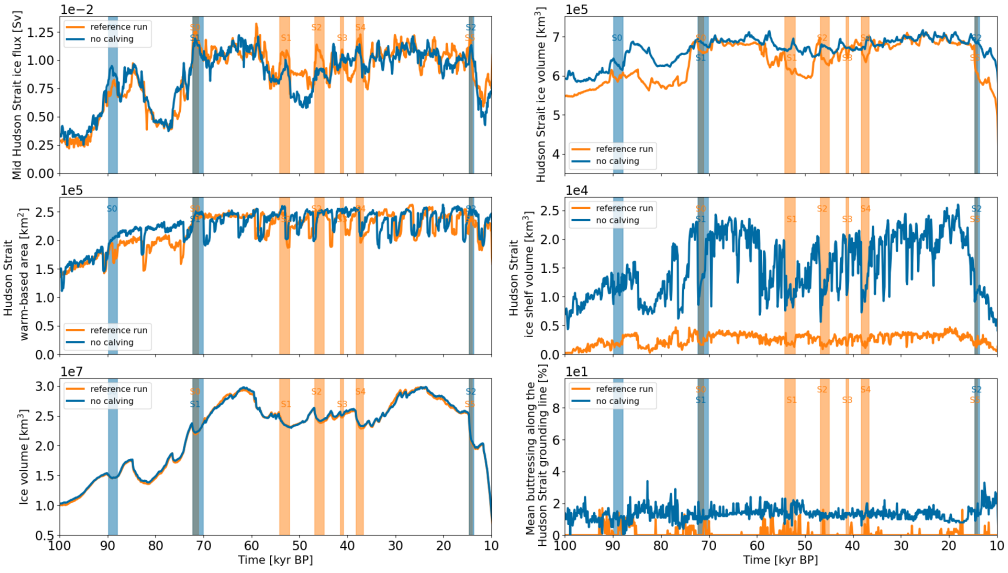

Figure S33. Time series of parameter vector 3 for the reference setup and a run without calving in the *ocean forcing area* after 100 kyr BP (BE_4 in Sec. 2.5.3). Otherwise as Fig. 4.

S6 GIA

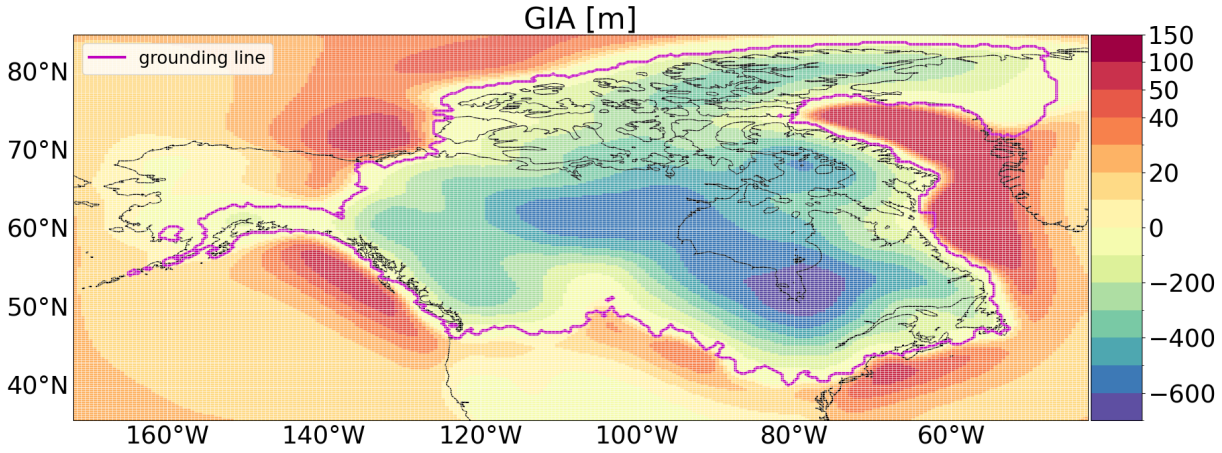

Figure S34. GIA for parameter vector 5 at 20 kyr BP compared to the bed topography at 120 kyr BP. The black contour is the present-day coastline provided by *cartopy* (Met Office, 2010 - 2015).

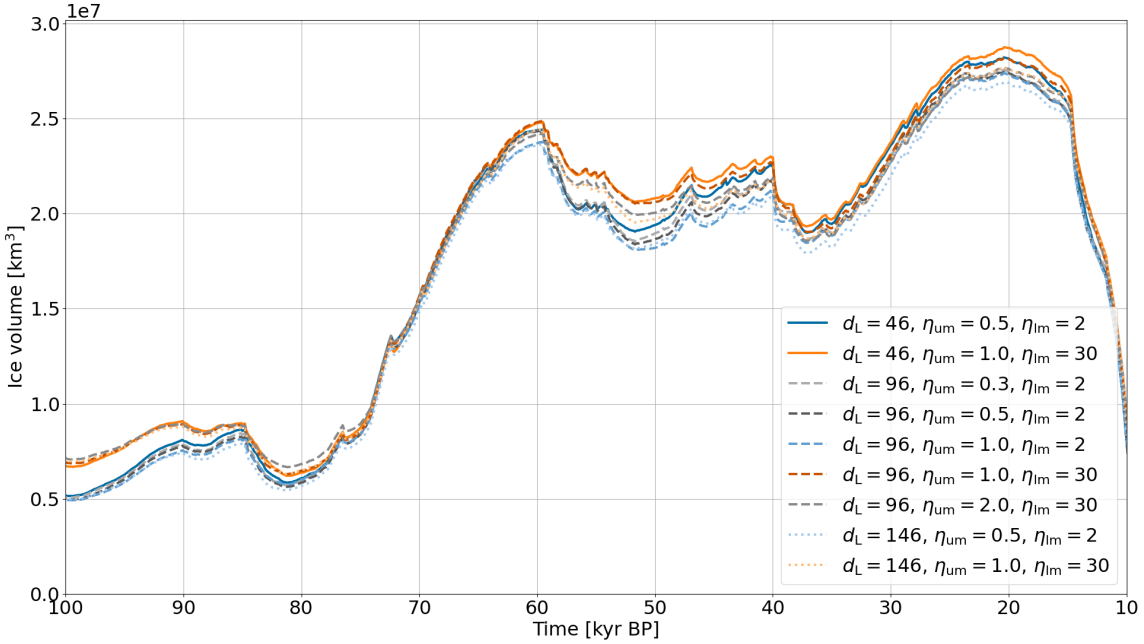

Figure S35. Mean North American ice volume across all 20 parameter vectors for 9 different earth rheology models of the global GIA model. d_L, η_{um}, and η_{lm} are the thickness of the Lithosphere (km), the viscosity of the upper mantle and the viscosity of the lower mantle (10^{21} Pa s), respectively.

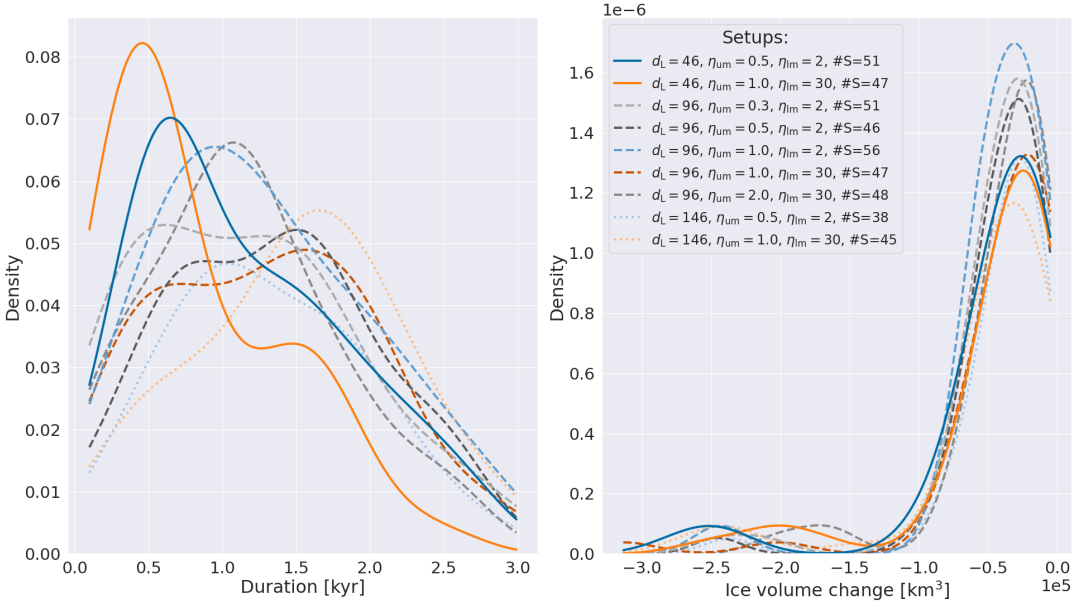

Figure S36. Kernel density plot for different earth rheologies when using the global GIA model. Each line is based on the surges within all runs with the same earth rheology model. d_{L}, η_{um}, and η_{lm} are the thickness of the Lithosphere (km), the viscosity of the upper mantle and the viscosity of the lower mantle (10^{21} Pa s), respectively. #S indicates the total number of surges across all runs of the sub-ensemble.

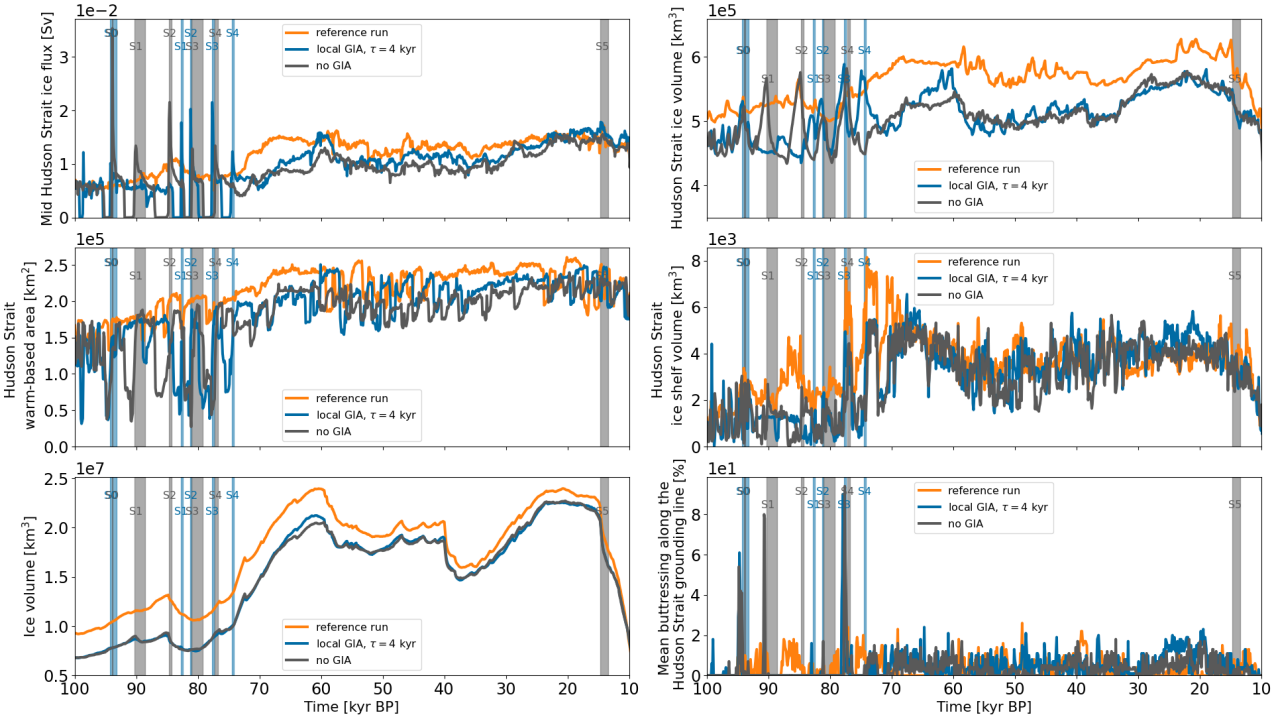

Figure S37. Time series of parameter vector 16 when using different GIA models. Otherwise as Fig. S7.

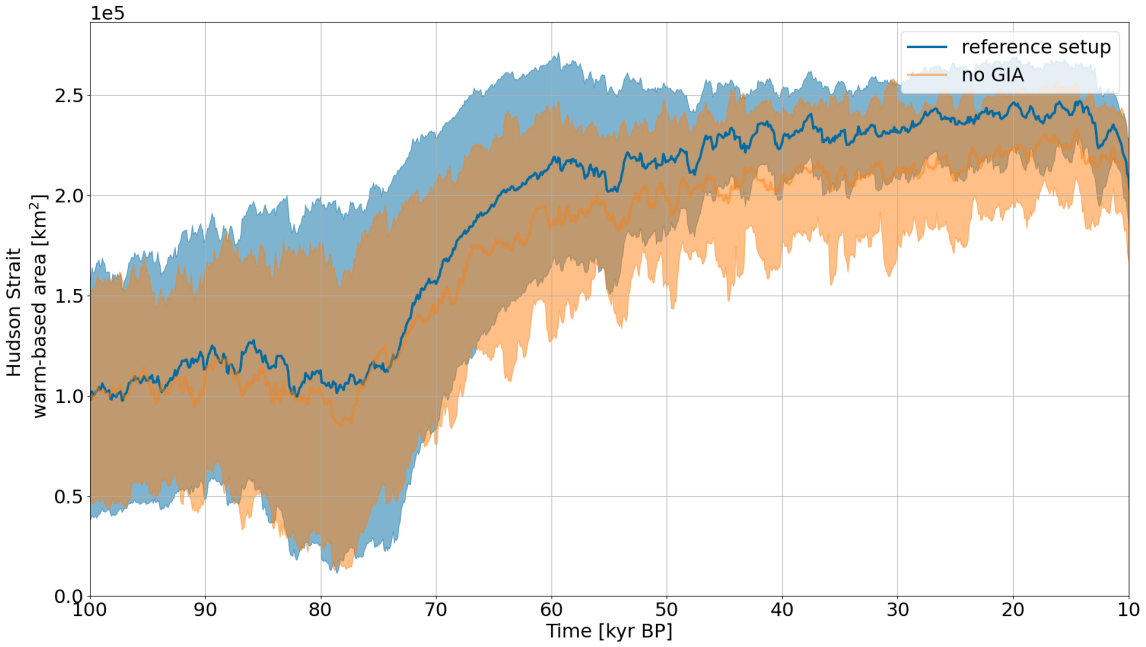

Figure S38. Hudson Strait warm-based area for the reference setup (global GIA model) and runs without GIA. The thick line represents the mean of the 20 run ensemble. The shaded area marks the minimum and maximum of the ensemble.

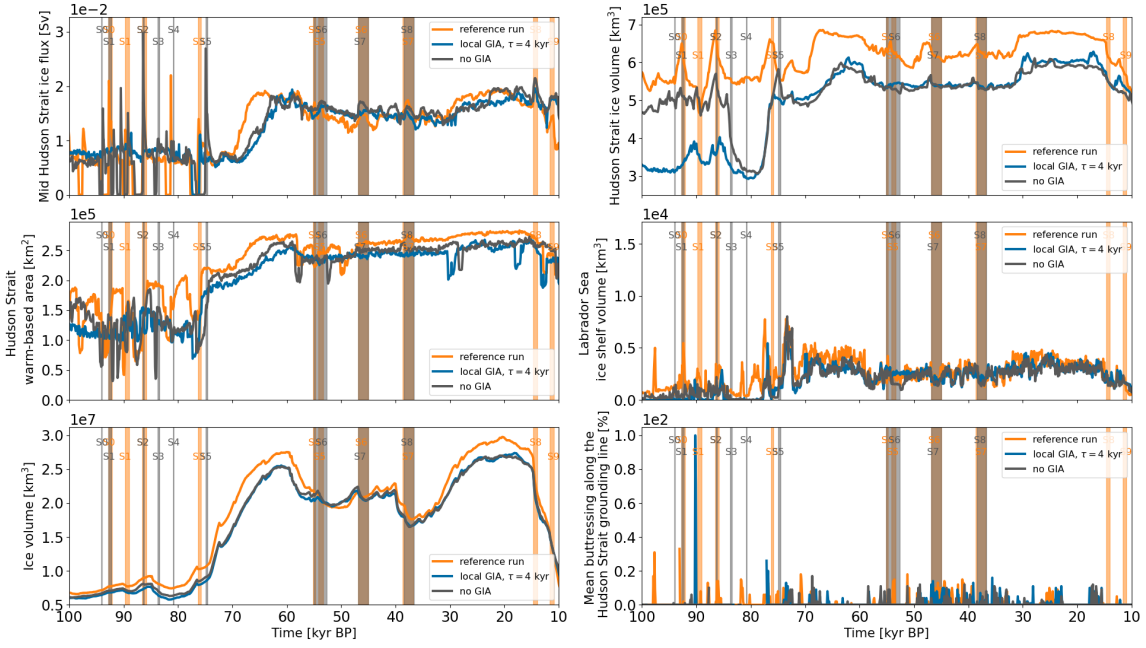

Figure S39. Time series of parameter vector 11 when using different GIA models. Otherwise as Fig. S7.

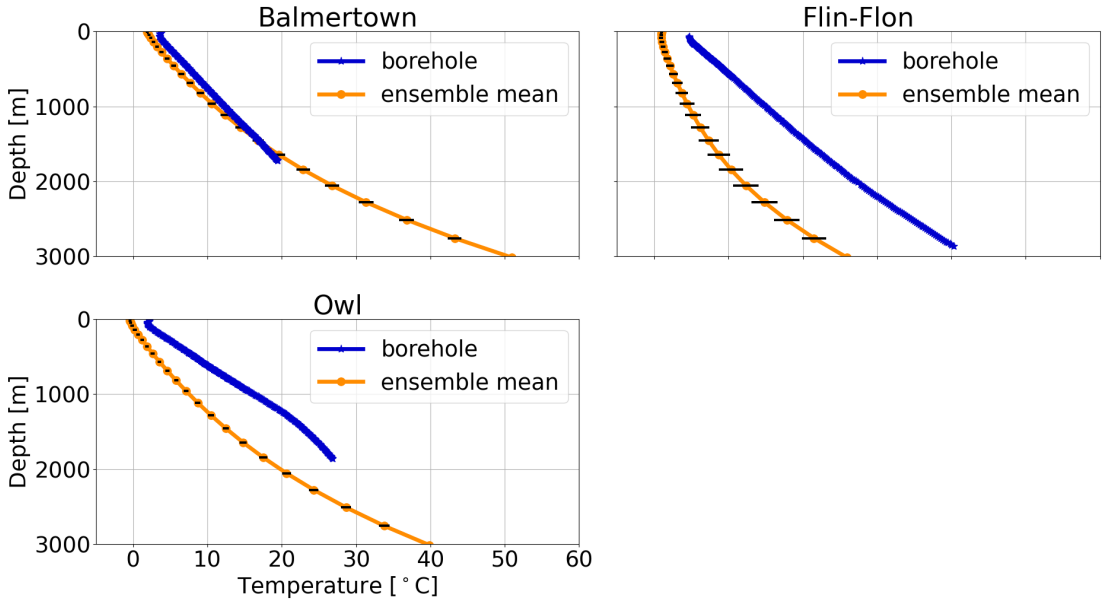

Figure S40. Bed temperature profiles for the Balmertown (93.7167°W, 51.0333°N, Rolandone et al., 2003), Flin-Flon (102.0°W, 54.717°N, J. C. Mareschal, personal communication, 2006), and Owl (97.86°W, 55.67°N, Rolandone et al., 2002) boreholes and the corresponding GSM grid cells. The location of the boreholes is shown in Fig. S41. The orange lines and black horizontal bars represent the present-day ensemble mean and standard deviation of the GSM reference setup (default GHF, Davies, 2013), respectively.

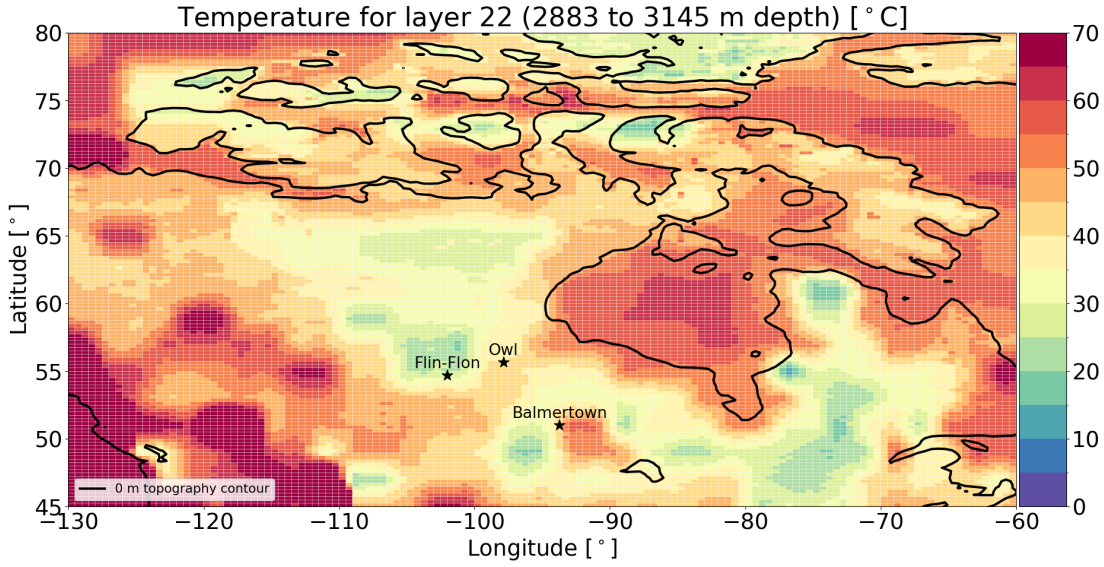

Figure S41. Bed temperature field between 2883 and 3145 m depth in the GSM. The default GHF was used (Davies, 2013). The black asterisks mark the locations of the boreholes shown in Fig. S40. The black contour line shows the present-day sea level used in the GSM

References

Bazin, L., Landais, A., Lemieux-Dudon, B., Toyé Mahamadou Kele, H., Veres, D., Parrenin, F., Martinerie, P., Ritz, C., Capron, E., Lipenkov, V., Loutre, M.-F., Raynaud, D., Vinther, B., Svensson, A., Rasmussen, S. O., Severi, M., Blunier, T., Leuenberger, M., Fischer, H., Masson-Delmotte, V., Chappellaz, J., and Wolff, E.: An optimized multi-proxy, multi-site Antarctic ice and gas orbital chronology (AICC2012): 120 - 800 ka, Climate of the Past, 9, 1715–1731, https://doi.org/10.5194/cp-9-1715-2013, 2013.

Blackwell, D. and Richards, M.: Geothermal Map of North America, AAPG Map, scale 1:6,500,000, Product Code 423, https://www.smu.edu/-/media/Site/Dedman/Academics/Programs/Geothermal-Lab/Graphics/Geothermal_MapNA_7x10in.gif, 2004.

Bradley, R.: PALEOCLIMATOLOGY (3rd edition), 2014.

Davies, J. H.: Global map of solid Earth surface heat flow, Geochemistry, Geophysics, Geosystems, 14, 4608–4622, https://doi.org/10.1002/ggge.20271, 2013.

Met Office: Cartopy: a cartographic python library with a Matplotlib interface, Exeter, Devon, https://scitools.org.uk/cartopy, 2010 - 2015.

Pollack, H. N., Hurter, S. J., and Johnson, J. R.: Heat flow from the Earth's interior: Analysis of the global data set, Reviews of Geophysics, 31, 267–280, https://doi.org/https://doi.org/10.1029/93RG01249, 1993.

Rolandone, F., Jaupart, C., Mareschal, J. C., Gariépy, C., Bienfait, G., Carbonne, C., and Lapointe, R.: Surface heat flow, crustal temperatures and mantle heat flow in the Proterozoic Trans-Hudson Orogen, Canadian Shield, Journal of Geophysical Research: Solid Earth, 107, ETG 7–1–ETG 7–19, https://doi.org/10.1029/2001jb000698, 2002.

Rolandone, F., Mareschal, J. C., and Jaupart, C.: Temperatures at the base of the Laurentide Ice Sheet inferred from borehole temperature data, Geophysical Research Letters, 30, 18–21, https://doi.org/10.1029/2003GL018046, 2003.

Tarasov, L. and Goldstein, M.: Assessing uncertainty in past ice and climate evolution: overview, stepping-stones, and challenges, Climate of the Past Discussions, 2021, 1–54, https://doi.org/10.5194/cp-2021-145, 2021.

Veres, D., Bazin, L., Landais, A., Toyé Mahamadou Kele, H., Lemieux-Dudon, B., Parrenin, F., Martinerie, P., Blayo, E., Blunier, T., Capron, E., Chappellaz, J., Rasmussen, S. O., Severi, M., Svensson, A., Vinther, B., and Wolff, E. W.: The Antarctic ice core chronology (AICC2012): an optimized multi-parameter and multi-site dating approach for the last 120 thousand years, Climate of the Past, 9, 1733–1748, https://doi.org/10.5194/cp-9-1733-2013, 2013.